Heliyon 7 (2021) e06275

Contents lists available at ScienceDirect

Heliyon

journal homepage: www.cell.com/heliyon

Research article

Reduction of Sb(V) by coupled biotic-abiotic processes under sulfidogenic conditions

Clayton R. Johnson [a], Dionysios A. Antonopoulos [a], Maxim I. Boyanov [a,b], Theodore M. Flynn [a,1], Jason C. Koval [a], Kenneth M. Kemner [a], Edward J. O'Loughlin [a,*]

[a] Biosciences Division, Argonne National Laboratory, Lemont, IL 60439-4843
[b] Bulgarian Academy of Sciences, Institute of Chemical Engineering, Sofia, 1113, Bulgaria

ARTICLE INFO

Keywords:
Antimony
Biogeochemistry
Dissimilatory sulfate reduction
Microbial reduction
Iron sulfide

ABSTRACT

Increasing use and mining of antimony (Sb) has resulted in greater concern involving its fate and transport in the environment. Antimony(V) and (III) are the two most environmentally relevant oxidation states, but little is known about the redox transitions between the two in natural systems. To better understand the behavior of antimony in anoxic environments, the redox transformations of Sb(V) were studied in biotic and abiotic reactors. The biotic reactors contained Sb(V) (2 mM as $KSb(OH)_6$), ferrihydrite (50 mM Fe(III)), sulfate (10 mM), and lactate (10 mM), that were inoculated with sediment from a wetland. In the abiotic reactors, The interaction of Sb(V) with green rust, magnetite, siderite, vivianite or mackinawite was examined under abiotic conditions. Changes in the concentrations of Sb, Fe(II), sulfate, and lactate, as well as the microbial community composition were monitored over time. Lactate was rapidly fermented to acetate and propionate in the bioreactors, with the latter serving as the primary electron donor for dissimilatory sulfate reduction (DSR). The reduction of ferrihydrite was primarily abiotic, being driven by biogenic sulfide. Sb and Fe K-edge X-ray absorption near edge structure (XANES) analysis showed reduction of Sb(V) to Sb(III) within 4 weeks, concurrent with DSR and the formation of FeS. Sb K-edge extended X-ray absorption fine structure (EXAFS) spectroscopy analysis indicated that the reduced phase was a mixture of S- and O-coordinated Sb(III). Reduction of Sb(V) was not observed in the presence of magnetite, siderite, or green rust, and limited reduction occurred with vivianite. However, reduction of Sb(V) to amorphous Sb(III) sulfide occurred with mackinawite. These results are consistent with abiotic reduction of Sb(V) by biogenic sulfide and reveal a substantial influence of Fe oxides on the speciation of Sb(III), which illustrates the tight coupling of Sb speciation with the biogeochemical cycling of S and Fe.

1. Introduction

Antimony (Sb) is a Group 15 metalloid found in a broad range of aquatic and terrestrial environments (Filella et al., 2009; Herath et al., 2017; He et al., 2018), typically at relatively low concentrations (e.g., ~0.2 mg kg^{-1} within the Earth's crust and 1 μg L^{-1} in fresh waters (Filella et al., 2002; Anderson 2012)). However, large deposits of Sb are relatively common, especially within areas of China (Anderson 2012), which in 2018 accounted for >60% of the 147,000 metric tons of Sb mined globally (USGS, 2020). Antimony trioxide (Sb_2O_3) is the most widely produced Sb compound, the majority of which is used as a flame retardant; however, Sb is also used in lead-acid batteries, semiconductors, paint pigments, pesticides, ammunition, and medicine (Dupont et al., 2016). The production, use, and disposal of these Sb-containing products, along with the initial mining of the element, can lead to environmental pollution (Scheinost et al., 2006; Murciego et al., 2007; Courtin-Nomade et al., 2012; Ritchie et al., 2013; Zhuang et al., 2018; Park et al., 2021), which has caused the United States Environmental Protection Agency to set forth maximum contaminant levels of 6 μg L^{-1} due to Sb's acute toxicity (Filella et al., 2002; Herath et al., 2017). The toxicity of Sb is dependent on its oxidation state, which can vary from –III, 0, III, and V (Filella et al., 2009), however, Sb(III) and Sb(V) are the most common in surface and near-surface environments and are also the most toxic, with Sb(III) being more toxic than Sb(V) (Filella and May 2003).

Although the toxicity of Sb is similar to that of arsenic (As)—another Group 15 element—their redox behavior is substantially dissimilar,

* Corresponding author.
E-mail address: oloughlin@anl.gov (E.J. O'Loughlin).
[1] Present address: Delta Science Program, Delta Stewardship Council, Sacramento, CA 95814.

https://doi.org/10.1016/j.heliyon.2021.e06275
Received 16 December 2020; Received in revised form 26 January 2021; Accepted 9 February 2021

which can result in differential mobility and compartmentalization in environmental systems (Mitsunobu et al., 2006; Warnken et al., 2017; Arsic et al., 2018). There has been a growing interest in understanding Sb redox transformations, particularly between the III and V oxidation states, to better determine the mobility and fate of Sb in natural and engineered systems. Currently, the biotic and abiotic processes controlling Sb redox transformations in both engineered and environmental systems are poorly understood (Herath et al., 2017; He et al., 2018). Field and laboratory studies indicate that the speciation/mobility of Sb in saturated soils, lacustrine sediments, and geothermal springs is linked to the biogeochemical cycling of Fe and S (Ullrich et al., 2013; Hockmann et al., 2014; Couture et al., 2015; Tandy et al., 2017; Arsic et al., 2018; Karimian et al., 2018; Ren et al., 2019; Johnston et al., 2020). However, there are substantial gaps in our understanding of the mechanisms by which coupled biotic and abiotic processes involved in the redox transformations of Fe and S determine the speciation/mobility and fate of Sb in natural systems. Both Fe(III) and Fe(II) minerals are highly reactive in geological systems and have been shown to participate in sorption and redox reactions with Sb (Tighe et al., 2005; McComb et al., 2007; Mitsunobu et al., 2010; Guo et al., 2014; Shangguan et al. 2015, 2016; Okkenhaug et al., 2016; Tandy et al., 2017). Sb adsorption to iron minerals, such as Fe(III) oxides and jarosite, affects the mobility of Sb and is dependent on redox conditions, Sb speciation, and pH (Leuz et al., 2006; Bolanz et al., 2013; Vithanage et al., 2013; Qi and Pichler 2017; Karimian et al., 2018). In particular, Sb(III) adsorbs strongly to Fe(III) oxides in soil and groundwater systems (Shangguan et al. 2015, 2016; Okkenhaug et al., 2016; Tandy et al., 2017), which can lead to oxidation to Sb(V) (Belzile et al., 2001; Leuz et al., 2006; Qi and Pichler 2016). Compared to Fe(III) oxides, little is known regarding the interactions of Sb with Fe(II)-bearing minerals. Green rust (a mixed ferrous/ferric layered double hydroxide) is an effective sorbent (and potential reductant) for Sb(V) (Mitsunobu et al. 2008, 2009) and the mixed ferric/ferrous mineral magnetite readily reduces Sb(V) to Sb(III) (Kirsch et al., 2008). Ferrous sulfide minerals (e.g., mackinawite) and dissolved sulfide species are also effective in reducing Sb(V) to Sb(III) (Kirsch et al., 2008; Polack et al., 2009), typically resulting in the formation of Sb_2S_3; however, Sb(III) can also remain in solution as aqueous sulfide complexes under sulfidic conditions, particularly in geothermal waters (Planer-Friedrich and Scheinost 2011).

Microbial activity is a key driver of the speciation and mobility of Sb in aquatic and terrestrial environments (Filella et al., 2007; Oremland 2016; He et al., 2018). Over 60 Sb(III)-oxidizing bacteria spanning 17 genera have been identified (Li et al., 2016). In the majority of these species, oxidation of Sb(III) to Sb(V) is linked to an enzymatic process for detoxification; however, at least two species have been shown to link Sb(III) oxidation to chemoautotrophic growth (Lialikova 1974; Terry et al., 2015). Several bacteria capable of using Sb(V) as a terminal electron acceptor for anaerobic respiration have been identified in both pure culture or as members of enriched microbial consortia (Nguyen and Lee 2014; Lai et al., 2016; Abin and Hollibaugh 2017; Nguyen et al. 2018, 2019; Zhu et al., 2018; Zhang and Hu 2019; Yang et al., 2020), as well as an archaeon that can use Sb(V) as an electron acceptor for anaerobic methane oxidation (Lai et al., 2018). In addition to direct microbial redox transformations of Sb(III) and Sb(V), microbial processes can indirectly impact Sb speciation/mobility by altering the geochemical conditions of their environment, particularly microbes involved in the biogeochemical cycling of Fe and S. For example, reductive dissolution of Fe(III) oxides by dissimilatory Fe(III)-reducing bacteria (DIRB) could lead to release of sorbed Sb(V) and potential reduction to Sb(III) by Fe(II)-bearing secondary minerals such as magnetite (Kirsch et al., 2008) or incorporation of Sb(V) into more crystalline secondary Fe(III) oxides (Burton et al., 2019). Likewise, microbial reduction of oxidized S species such as sulfate, sulfite, and thiosulfate results in the formation of sulfide, which in addition to being a potential electron donor for the reduction of Sb(V) to Sb(III), can provide an efficient sink for Sb(III) via the formation of sparingly soluble Sb_2S_3 (Wang et al., 2013; Kulp et al., 2014; Zhu et al., 2018). Indeed, immobilization of Sb under sulfidogenic conditions created by stimulation of dissimilatory sulfate-reducing bacteria (DSRB) has been proposed as an effective approach for remediation of Sb contaminated wastewaters (Wang et al., 2013; Zhang et al., 2016; Liu et al., 2018; Zhu et al., 2018).

The behavior of Sb in aquatic and terrestrial environments can be influenced by biogeochemical processes involving Fe and S. However, a comprehensive understanding of the coupling of biotic and abiotic redox reactions of Sb, Fe, and S in anoxic environments is lacking, particularly with respect to the involvement of Fe transformations under sulfidogenic conditions. To better understand the behavior of antimony under anoxic conditions, we used X-ray absorption fine structure (XAFS) spectroscopy to examine the transformations of Fe(III) and Sb(V), and 16S rDNA analysis to determine the changes in microbial populations under sulfidogenic conditions in bioreactors containing Sb(V), Fe(III) oxide (ferrihydrite), sulfate, lactate, and wetland sediment. We also examined the interaction of Sb(V) with green rust, magnetite, siderite, vivianite or mackinawite to assess the potential for abiotic reduction of Sb(V) to Sb(III) by these Fe(II)-bearing secondary minerals commonly formed during microbial Fe(III) and sulfate reduction.

2. Experimental section

2.1. Defined mineral medium (DMM)

The DMM consisted of 5.0 mM NH_4Cl, 1.0 mM KCl, 0.1 mM CaCl, 0.1 mM $MgSO_4$, 1.0 mM NaH_2PO_4, 15 mM HEPES buffer, 15 mM PIPES buffer (disodium salt), 10 mL L^{-1} of Wolfe's vitamin solution, and 5 mL L^{-1} of trace metals solution (which was added after all of the other components were combined). The pH of the DMM was adjusted to pH 7.2, followed by filter sterilization using a 0.2 μm pore-size cellulose nitrate membrane. The trace metal solution (Wolin et al., 1963) consisted of (g L^{-1}) nitrilotriacetic acid (1.5), $MnSO_4 \bullet H_2O$ (0.5), $FeSO_4 \bullet 7H_2O$ (0.1), $CoCl_2 \bullet 6H_2O$ (0.1), $ZnSO_4 \bullet 7H_2O$ (0.1), $CuSO_4 \bullet 5H_2O$ (0.1), $AlK(SO_4)_3 \bullet 12H_2O$ (0.01), H_3BO_3, (0.01), and $Na_2MoO_4 \bullet 2H_2O$ (0.01), with the addition of $NiCl_2 \bullet 6H_2O$ (0.05), $Na_2SeO_3 \bullet 5H_2O$ (0.263), and $Na_2WO_4 \bullet 2H_2O$ (0.025) and was titrated to pH 6.2 with 1 M KOH. Wolf's vitamin solution (Wolin et al., 1963) consisted of (mg L^{-1}) biotin (2.0), folic acid (2.0), pyridoxine HCl (10.0), thiamine HCl (5.0), riboflavin (5.0), nicotinic acid (5.0), d-pantothenic acid-hemicalcium salt (5.0), cyanocobalamin (0.1), p-aminobenzoic acid (5.0), and thioctic acid (5.0) and was adjusted to pH 7.0.

2.2. Ferrihydrite synthesis

Ferrihydrite was prepared as described by Schwertmann and Cornell (2000) by titrating 0.5 M $FeCl_3$ with 1.0 M KOH to pH 7.5. The precipitate was repeatedly washed with water (18 Mohm-cm). The washed ferrihydrite was used to prepare a stock suspension containing 200 mM Fe.

2.3. Sulfidogenic microcosms

The behavior of Sb(V) under sulfidogenic conditions was examined in microcosms prepared in autoclaved serum bottles (240 mL capacity) containing 125 mL of DMM, 20 mL of 20 mM $KSb(OH)_6$, 2.0 mL of 1.0 M $NaSO_4$, 50 mL of 200 mM Fe(III) (as ferrihydrite), and 2.0 mL of 2.0 M lactate. In systems where select components were not added, a final volume of 199 mL was achieved by adding the necessary amount of distilled water (sterile controls were prepared to a final volume of 200 mL). All systems were sealed with sterile butyl rubber plugs and aluminum crimp caps and sparged for 20 min with sterile Ar gas to remove O_2 from the solution and headspace. The bioreactors were inoculated with 1.0 mL of the inoculum slurry (described below) using a sterile needle and syringe. Four different experimental systems were prepared in duplicate (with the exception of system C) and designated as: (A) Sb(V), Fe(III), and sulfate

(uninoculated); (B) Fe(III) and sulfate; (C) Sb(V) and sulfate; and (D) Sb(V), Fe(III), and sulfate. The bioreactors were incubated in the dark at 30 °C with continuous mixing on a roller drum. Routine sampling involved the removal of 1.5 mL of suspension, of which 0.25 mL was added to 0.75 mL of 1 M HCl for subsequent Fe(II) measurement. The remaining suspension was centrifuged at 25,000 × g for 10 min. After centrifugation, 0.1 mL of supernatant was combined with 0.9 mL of 15% (v:v) isopropanol and saved for sulfate analysis; 0.1 mL of supernatant was mixed with 0.9 mL of 5 mM H_2SO_4 and saved for organic anion analysis; and the remaining supernatant was used for pH measurement. Less frequently, 11 mL of suspension were collected, 1.5 mL of which was frozen at -80 °C for subsequent 16S rRNA-based microbial community analysis. The remaining suspension was filtered through 25 mm 0.2 μm pore-size nylon filters. The filtrate was saved for dissolved Sb analysis. The filters were placed between layers of Kapton film, double contained (sealed in a 50 mL centrifuge tube that was then enclosed in a Mason jar), and stored at -80 °C for subsequent Fe and Sb XAFS analysis. Sample collection and processing occurred in a glove box (Coy Laboratory Products, Grass Lake, MI, USA) containing an atmosphere of 3–5% H_2 in N_2 (v:v) with a Pd catalyst to maintain O_2 in the box <1 ppm at all times.

2.4. Preparation of the inoculum

The inoculum used in the sulfidogenic microcosms was prepared from the top 5 cm of sediment collected from the edge of a shallow, *Typha* (cattail)-dominated wetland at Argonne National Laboratory, Lemont, IL, USA. A sediment slurry was prepared by adding 10 g of sediment to 150 mL of the DMM in a sterile 160-mL serum bottle that was then sealed and made anoxic as described above.

2.5. Enrichment for Sb(V)Reducing bacteria

Cultures for enrichment of Sb(V)-reducing bacteria were prepared in Balch tubes containing 10 mL of DMM amended with 2 mM $KSb(OH)_6$, and 5 mM of either lactate, acetate, or propionate. The tubes were sealed with sterile butyl rubber plugs and aluminum crimp caps, sparged for 20 min with sterile Ar gas, inoculated with 0.2 mL of inoculum, and incubated at 30 °C in the dark. Serial transfers were made after incubating for 7 days.

2.6. Synthesis of Fe(II)-Bearing minerals

Hydroxysulfate green rust was synthesized by air oxidation of a 1.0 M ferrous sulfate solution as described by O'Loughlin and Burris (2004). pXRD analysis of the solids was consistent with sulfate green rust (Figure 1). The green rust was maintained as an aqueous suspension. Magnetite (Fe_3O_4) was prepared using the method of Schwertmann and Cornell (2000). Briefly, 80 g of $FeSO_4 \bullet 7H_2O$ were dissolved in 560 mL of anoxic distilled water. The resulting solution was transferred to a 1.5 L 90 °C water-jacketed reaction flask with continuous purging with Ar. Once the Fe(II) solution reached 90 °C, 240 mL of an anoxic solution containing 6.46 g of KNO_3 and 44.9 g of KOH was added dropwise over 5 min, after which the resulting black suspension was kept mixed and maintained at 90 °C for 1 h. After cooling to ambient temperature, the suspension was transferred to an anoxic glovebox and washed repeatedly with anoxic distilled water and maintained as an aqueous suspension. pXRD analysis of the solids was consistent with magnetite (Figure 1).

Siderite ($FeCO_3$) and vivianite ($Fe_3(PO_4)_2 \bullet 8H_2O$) were both synthesized from a 0.5 M Fe(II) solution prepared by dissolving 140 g of $FeSO_4 \bullet 7H_2O$ in 1 L of distilled water in an anoxic glove box. The solution was titrated to pH 7 with 1 M NaOH, during which small amounts of a dark blue-green precipitate formed and were removed by filtration with a 0.2 μm nylon membrane filter (this procedure removes trace Fe(III) introduced with the $FeSO_4$ reagent). Siderite was prepared by the dropwise addition of 40 mL of the circumneutral 0.5 M Fe(II) solution to 400 mL of 0.5 M $NaHCO_3$ with constant mixing with a magnetic stirrer. The white precipitate was washed repeatedly with anoxic distilled water and maintained as an aqueous suspension. The solids were identified as siderite based on pXRD (Figure 1). Vivianite was prepared by the dropwise addition of 60 mL of the circumneutral 0.5 M Fe(II) solution to 100 mL of 0.1 M Na_2HPO_4 with constant mixing with a magnetic stirrer. The white precipitate was washed repeatedly with anoxic distilled water and maintained as an aqueous suspension. pXRD analysis of the solids was consistent with vivianite (Figure 1). Both the siderite and vivianite were maintained as hydrated suspensions.

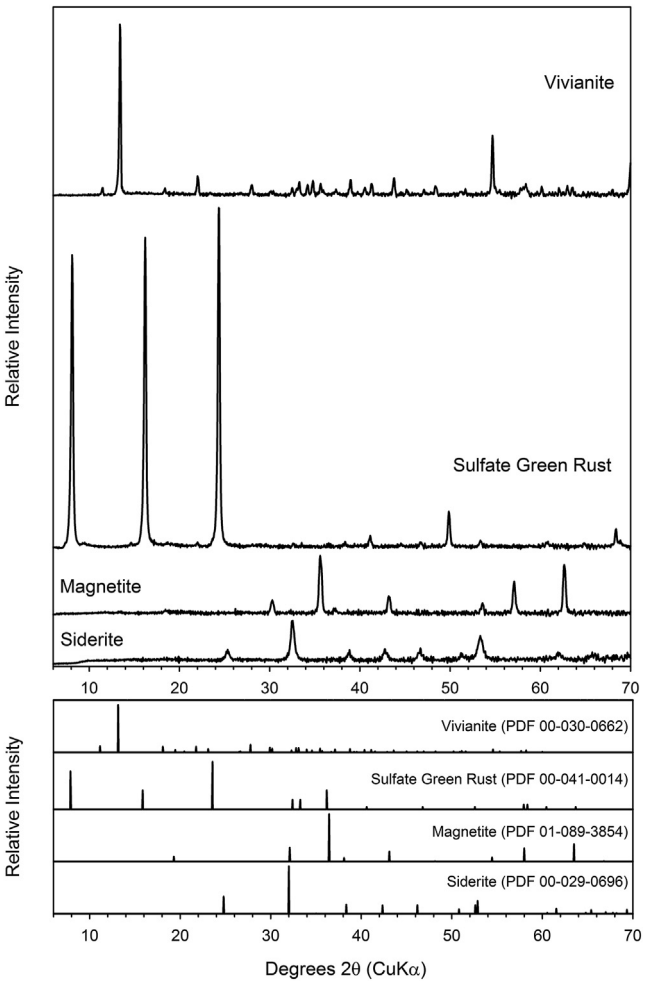

Figure 1. pXRD analysis of the vivianite, sulfate green rust, magnetite, and siderite used in this study.

Mackinawite (FeS) was prepared as described by Patterson et al. (1997) Equal volumes of 1.0 M $FeCl_2$ and 1.0 M Na_2S solutions in 0.1 M NaCl were mixed at a constant rate of 0.5 L min^{-1}. A black precipitate formed immediately and was allowed to settle. The precipitate was washed repeatedly with 0.1 M NaCl until the Fe(II) concentration in the rinsate was below 10 μM pXRD analysis of the solids was consistent with poorly-crystalline mackinawite (Figure 2). The FeS was maintained as a hydrated suspension.

2.7. Sb(V) interactions with Fe(II)-Bearing minerals

The potential for abiotic reduction of Sb(V) by Fe(II)-bearing minerals was examined in sterile 160-mL serum bottles containing 50 mL of DMM amended with 2 mM $KSb(OH)_6$ and 50 mM Fe(II) as either magnetite, green rust, siderite, vivianite, or mackinawite. An additional system was prepared by adding 2 mM $KSb(OH)_6$ to 50 mL of pasteurized (1 h at 70 °C) suspension removed from one of the system B bioreactors at 21 d after inoculation. The experimental systems were prepared in a glove box containing an anoxic atmosphere, sealed with sterile butyl rubber plugs

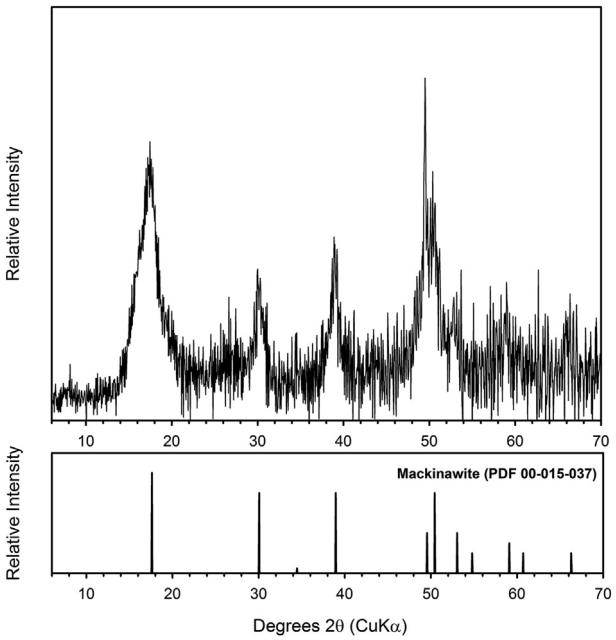

Figure 2. pXRD analysis of the mackinawite used in this study.

and aluminum crimp caps, and sparged with sterile Ar gas for 20 min to provide an inert atmosphere. After 21 d, samples were collected to determine the concentration of Sb remaining in solution and the oxidation state of solid phase Sb by XAFS using two different approaches depending on the anticipated concentration of Sb in the solids. Samples that were expected to have relatively high solid phase Sb concentrations were prepared as filter mounts using the procedure described previously for the microcosm samples. Samples expected to have lower Sb concentrations were prepared by centrifuging the suspensions and mounting the hydrated pellets in holes machined in Plexiglass slide-mount sample holders that were covered with Kapton film secured with Kapton tape. Filtrate or supernatant was saved for dissolved Sb analysis.

2.8. Chemical analyses

The reduction of ferrihydrite was assessed by measuring the Fe(II) in the suspensions by acid extraction and analysis by the ferrozine method (Stookey 1970) using HEPES-buffered ferrozine reagent (Sørensen 1982) as described by O'Loughlin et al. (2019). Sulfate reduction was monitored by measuring sulfate concentration using the method of Kolmert et al. (2000), scaled for 0.5 mL of sample. Briefly, 0.5 mL of sample was combined with 0.5 mL of conditioning reagent and 30 mg of $BaCl_2$ powder was added and the mixture was immediately mixed (vortexed) for 30 s. Immediately after mixing, the mixture was poured into a microcuvette and the absorbance at 430 nm was measured; the detection limit was 0.2 mM SO_4^{2-}. Aqueous phase Sb concentrations were determined by inductively coupled plasma-optical emission spectroscopy (ICP-OES) using a PerkinElmer 4300DV instrument. Measurement of the Sb emission line at 217.582 nm in radial view mode provided a detection limit of 5 μM. An Agilent 1100 series high performance liquid chromatograph (HPLC) was used to determine the concentrations of acetate, lactate, and propionate as described by Kwon et al. (2014). The pH of aqueous solutions was measured using a Semi Micro pH electrode (Thermo Scientific Inc.) calibrated with NIST-traceable pH standards to a precision of 0.01 pH units.

2.9. pXRD analysis

The identity of the crystalline phases was determined by powder X-ray diffraction (pXRD) analysis. Samples were measured as either dried powders packed into sample holders or as wet pastes collected by filtration on nylon membrane filters (25-mm diameter, 0.22-μm pore size) and covered with 8.4-μm-thick Kapton film. Materials stable under oxic conditions were scanned between 5° and 80° 2θ at a speed of 0.2° 2θ min^{-1} using a Rigaku MiniFlex X-ray diffractometer with a Ni-filtered Cu Kα radiation source, while samples of O_2-sensitive materials were scanned at a speed of 1° 2θ min^{-1} and showed no evidence of oxidation during the course of the measurement. The JADE 9 software package (MDI, Livermore, CA) was used to remove the background and the $K_{\alpha 2}$ components.

2.10. 16S rRNA-Based microbial community analysis

DNA was extracted from the samples collected for microbial community analysis as described by Kwon et al. (2014). Amplicon libraries of 16S rRNA genes from organisms in these samples were generated using the polymerase chain reaction (PCR). Primers targeted the V4 region of this gene in both bacteria and archaea (515F and 806R) (Bates et al., 2011; Caporaso et al., 2011). The reverse primer was Golay-barcoded to allow for sample multiplexing during sequencing on the Illumina MiSeq platform (Caporaso et al., 2012). PCR reactions for each sample were performed in triplicate using 5 PRIME MasterMix (Gaithersburg, MD). PCR reaction conditions were as follows: initial denaturing by heating to 95 °C for 3 min followed by 35 cycles at 95 °C for 30 s, 50 °C for 45 s, then 72 °C for 90 s. Amplification was finalized with a final extension step at 72 °C for 10 min. No amplification was observed in negative (template DNA-free) control reactions. Primer dimers were removed using the UltraClean PCR Clean-Up Kit (MO BIO Laboratories, Inc.), and the amount of DNA in each pooled sample was measured using the Quant-iT PicoGreen dsDNA assay (Invitrogen). Prior to sequencing, the amount of DNA in each sample was normalized to a final concentration of 2 ng μL^{-1}.

Paired-end PCR amplicons were sequenced using the Illumina MiSeq platform at the Environmental Sample Preparation and Sequencing Facility at Argonne National Laboratory following the guidelines of the Earth Microbiome Project (Caporaso et al., 2012; Thompson et al., 2017).

A total of 4.48 million paired-end sequences were generated across 63 samples for an average sequencing depth of 71,104 sequences per sample. Paired-end reads were joined together using PEAR (Zhang et al., 2014), and sequences that could not be joined due to low quality scores were discarded. Barcoded sequences were demultiplexed in QIIME version 1.9.1 (Caporaso et al., 2010) using the *split_libraries_fastq.py* command and the default quality control parameters. Sequences were then dereplicated, filtered for chimeras, and clustered into OTUs at the 97% identity threshold using the UPARSE-OTU algorithm (Edgar 2013) as implemented in USEARCH version 11.0 (Edgar 2010). Singletons (OTUs represented by a single sequence across all samples) were discarded. The taxonomy of representative sequences from each OTU was classified using the UCLUST algorithm (Edgar 2010) based on the SILVA reference database version 132 (Quast et al., 2013). Alpha and beta diversity analyses were conducted using version 1.24.2 of the phyloseq package in R (McMurdie and Holmes 2013). Beta diversity comparisons were made using nonmetric multidimensional scaling (NMDS) based on the weighted UniFrac metric (Hamady et al., 2010; Lozupone et al., 2011). UniFrac distances were calculated based on a phylogenetic tree constructed using FastTree Price, 2010 #5975} from sequences aligned using PyNAST Caporaso, 2010 #5976}. Raw sequence data are publicly available through MG-RAST (Meyer et al., 2008) under project number 96966.

2.11. Fe and Sb XAFS analysis

Sb K-edge (30,491 eV) and Fe K-edge (7,112 eV) X-ray absorption near edge (XANES) and extended X-ray absorption fine-structure (EXAFS) (Boyanov and Kemner 2019) spectra were collected at ambient temperature at the MRCAT/EnviroCAT beamline at sector 10-BM (Kropf et al., 2010), Advanced Photon Source, Argonne National

Laboratory, Illinois, USA. To maintain the redox integrity of the samples, they were transported to the beamline under anoxic conditions and spectra were collected using a N_2-purged sample cell (O'Loughlin et al., 2003). The incident energy was scanned by using the Si(111) reflection of the double crystal monochromator in quick-scanning mode. The spectra were collected from several locations of the samples, in transmission or fluorescence mode using gas-filled ionization chambers. No differences in the spectra were observed at different locations or with irradiation time, so the final spectrum for each sample was produced by averaging all collected spectra. Energy calibration was maintained at all times by simultaneously collecting a spectrum from an Sb or Fe foil using X-rays transmitted through the samples. Standards for Sb XAFS analysis included $KSb(OH)_6$, Sb_2O_3-senarmontite, Sb_2O_3-valentinite, Sb_3O_6OH--stibiconite, Sb_2O_4-cervantite, Sb_2O_5, Sb_2S_2O-kermesite, Sb_2S_3-amorphous, Sb_2S_3-stibnite, $FeSbO_4$-tripuhyite, $FeSb_2S_4$-berthierite, FeSbS-gudmundite, Sb_2S_5, Sb(III) sorbed on ferrihydrite, Sb(III)aq, and Sb(V)aq. Sources, characterization, and XAFS analysis of the Sb standards are provided in the Supporting Information; unless otherwise indicated, the standards were deposited on the adhesive side of Kapton tape to produce a thin, uniform layer and the tape was folded to produce a sample 16 to 32 layers thick.

Normalization and background subtraction of the measured spectra was done with the program AUTOBK (Newville et al., 1993). Data were Fourier transformed (FT) by using the FEFFIT program (Newville et al., 1995), using identical transform parameters for the standards and the unknown spectra (e.g., k-weighting, Fourier transformation ranges, and 1.0 $Å^{-1}$ Hanning window functions). Linear combination fits were performed with the program ATHENA (Ravel and Newville 2005). The shell-by-shell EXAFS analysis was carried out in R-space using the program FEFFIT (Newville et al., 1995). The crystal structures of tripuhyite (Berlepsch et al., 2003) and senarmontite (Whitten et al., 2004) were used for the calculation of the theoretical EXAFS paths using the program FEFF 8.2 (Ankudinov et al., 1998). Additional details on the methods used in the analysis packages can be found in the documentation of the corresponding program.

3. Results

3.1. Bioreactors

No changes were observed in the pH and the concentrations of lactate, sulfate, and Fe(II) in the uninoculated control (system A) (Figures 3 and 4). Solution phase Sb concentration decreased from 2 mM to 0.03 mM within 5 d, resulting in ~98% of the Sb associated with the solids. Analysis of the solids by Sb XANES indicated that there was no reduction of Sb(V) to Sb(III) (Figure S18). Furthermore, Sb EXAFS analysis of the solids (ferrihydrite) is consistent with sorption of antimonate by means of an inner-sphere complex (Figure S19), which corresponds with previous reports of antimonate sorption to Fe(III) oxides (Leuz et al., 2006; Scheinost et al., 2006; McComb et al., 2007; Mitsunobu et al., 2013).

Lactate was depleted within 5 d in the inoculated bioreactors containing ferrihydrite and sulfate (system B) (Figure 5). Consumption of lactate was accompanied by a decrease in pH from 7.00 to 6.91 (Figure 3) and the production of acetate and propionate, as well as production of 25 mM $Fe(II)_T$ and consumption of 5 mM sulfate (Figure 5). During this time the microbial populations in the bioreactors were dominated by members of the *Veillonellaceae* (38–45%), *Desulfovibrio* (30–33%), and *Sulfospirillum* (12–14%) (Figure 6). Further reduction of Fe(III) and sulfate resulted in the accumulation of 48 mM $Fe(II)_T$ and depletion of sulfate below the detection limit (0.2 mM) and was accompanied by decreases in propionate concentrations, increased acetate, increased pH (7.46), and a shift in dominant microbial populations to *Desulfovibrio* (36–39%), *Desulfobulbus* (21–27%), and *Geobacter* (17%) 21 d after inoculation. Over the course of the incubation the color of the solids changed from the red-brown color of ferrihydrite to black (Figure 7). Fe XANES analysis of the solids indicated that only 20% of the initial 50 mM Fe(III) remained after 21 d (Figure S20 and Table S9) with the remaining 80% present as Fe(II). pXRD analysis of the solids at 21 d clearly shows the presence of siderite (Figure 8) and linear combination (LC) fitting of the Fe EXAFS spectrum indicates that siderite comprised 52% of the Fe, with the remainder consisting of mackinawite (26%) and magnetite (22%) (Figure S21). The concentration of Fe(II) in the bioreactors indicated by XANES (40 mM) plus the $Fe(II)_{aq}$ concentration of 0.35 mM is significantly lower than the 48 mM determined by our $Fe(II)_T$ measurement. However, Kwon et al. (2014) have shown that acid digestion of samples consisting of defined mixtures of Fe(III) oxides and ferrous sulfide can generate additional Fe(II) by reduction of Fe(III) by free sulfide generated from the dissolution of FeS, suggesting that the $Fe(II)_T$ measurements based on acidification of the samples overestimated the extent of Fe(III) reduction in the bioreactors.

In system C (the bioreactor containing Sb(V) and sulfate), lactate concentrations decreased to below detection (50 μM) within 5 d, concurrent with a decrease in pH (Figure 3), production of acetate and propionate (Figure 9), and an increase in the *Veillonellaceae* from <1% to 94% (Figure 10). Sulfate concentration decreased from 10.28 to 5.33 mM over 21 d (Figure 9), accompanied by an increase in *Desulfovibrio* from

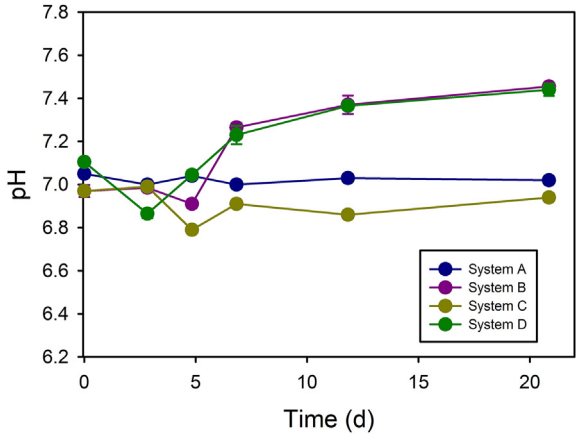

Figure 3. pH profiles of the microcosms: (A) Fe(III) and sulfate (uninoculated); (B) Fe(III) and sulfate; (C) Sb(V) and sulfate; and (D) Sb(V), Fe(III), and sulfate. Error bars indicate the standard error.

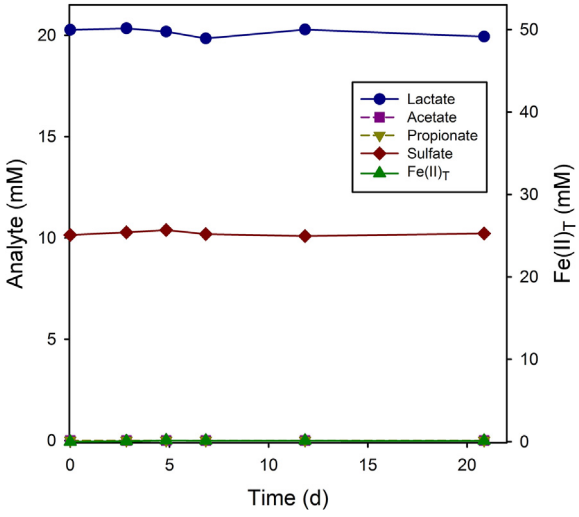

Figure 4. Concentration profiles of $Fe(II)_T$, sulfate, lactate, propionate, and acetate in system A [Fe(III) and sulfate (uninoculated)]. Error bars indicate the standard error are smaller than the symbol size.

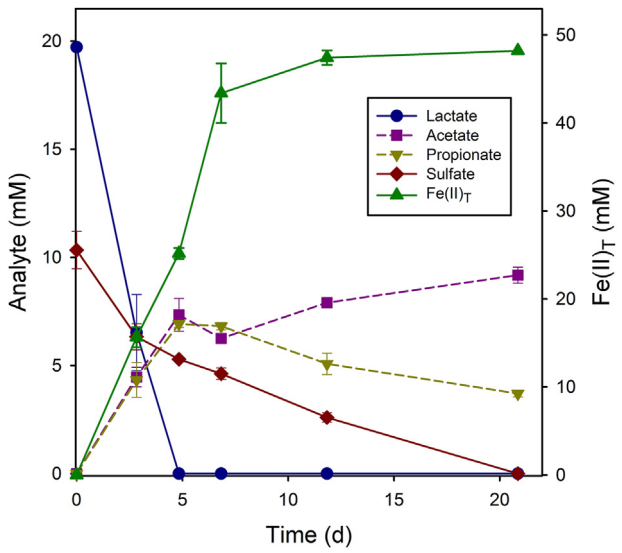

Figure 5. Concentration profiles of Fe(II)$_T$, sulfate, lactate, propionate, and acetate in system B [Fe(III) and sulfate] bioreactors. Error bars indicate the standard error.

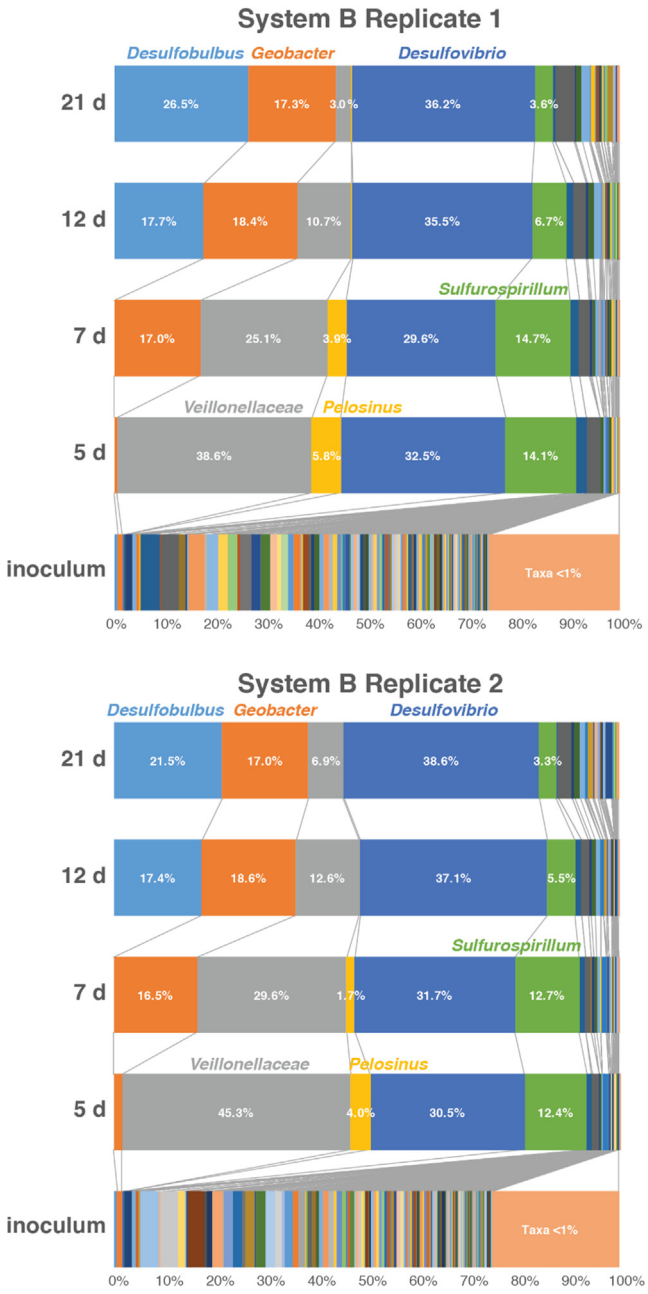

Figure 6. Changes in 16S rRNA gene-based community composition highlighting populations that are >5% at any time in system B [Fe(III) and sulfate].

<1% to 6% (Figure 10). Within 5 d of inoculation, the concentration of Sb(V)aq decreased by ~50% from 2 to 1 mM (Figure 11) and Sb XANES analysis indicated that the solids-associated Sb consisted of 55% Sb(V) and 45% Sb(III) (Figure S23 and Table S10). At 12 d Sb(V)aq decreased to 0.7 mM and the Sb(III) content of the solids increased to 79%. There was little change in the distribution of Sb between 12 and 21 d. However, after 1 y, more than 95% of the Sb was solids-associated Sb(III). The Sb EXAFS data show that over time the speciation of the solids-associated Sb shifts from an Sb(V) species similar to $KSb(OH)_6$ to amorphous Sb(III)-sulfide (Figure 12 and Figure S23). The spectra from different sampling times cross at multiple isosbestic points, indicating that the transformation is occurring predominantly between the two endmember species. There was no replicate bottle of system C in our initial experiment, however, results from a repeat of the experiment involving duplicate system C bioreactors indicated complete reduction of Sb(V) to amorphous Sb(III) sulfide within 5 months (Figure S24).

As in systems B and C, lactate was depleted within 5 d in system D (the bioreactor containing Sb(V), Fe(III), and sulfate), with the production of acetate and propionate (Figure 13) and an initial decrease in pH from 7.11 to 6.87 at 3 d, which then increased to 7.05 by 5 d (Figure 3). Consumption of lactate was accompanied by production of 7.7 mM Fe(II)$_T$ and a 1.9 mM decrease in sulfate concentration (Figure 13), considerably less than the production of 25 mM Fe(II)$_T$ and consumption of 5 mM sulfate during this same period in system B. As with system B, the microbial populations during lactate fermentation were dominated by members of the *Veillonellaceae* (66–71%), *Desulfovibrio* (13%), and *Sulfospirillum* (10–11%) (Figure 14). Within 21 d, reduction of Fe(III) and sulfate resulted in the accumulation of 41 mM Fe(II)$_T$ and depletion of sulfate below the detection limit (0.2 mM) and was accompanied by decreases in propionate concentrations, increasing acetate concentrations, increased pH (7.44), and a shift in dominant microbial populations to *Desulfobulbus* (32–40%), *Geobacter* (29–32%), *Veillonellaceae* (10–14%), and *Desulfovibrio* (8–11%). Similar to system B, the color of the solids changed from the red-brown to black (Figure 7) accompanied by the reduction of 65% of Fe(III) to Fe(II) as determined by XANES spectroscopy, which is significantly less than the 82% reduction determined colorimetrically but likely represents the actual extent of reduction in situ due to the aforementioned overestimation of Fe(II) by acid extraction in sulfidogenic systems (Kwon et al., 2014). pXRD analysis of the solids at 21 d clearly shows the presence of siderite (Figure 8) and indications of mackinawite. LC fitting of the Fe EXAFS spectrum indicates that siderite comprises 59% of the Fe, with the remainder consisting of mackinawite (18%) and ferrihydrite (23%) (Figure S22, Table S9). Sb was rapidly removed from solution in system D, with >99% associated with the solids within 5 d (Figure 15). Sb XANES analysis of the solids-associated Sb indicates a progressive reduction of Sb(V) to Sb(III) over the initial 21 d of incubation reaching complete reduction to Sb(III) within 98 d (Figure S25). Sb EXAFS analysis of the same samples shows a change in Sb(III) speciation over time (Figure 16). The spectral shape of the 21-day sample is very similar to that of Sb(III) adsorbed to ferrihydrite. Further incubation results in a change in the spectrum at 98 d towards the features of the Sb_2S_3 standard. Linear combination fits of the spectra indicate a fast initial transformation from the Sb(V) species to adsorbed, O-coordinated Sb(III) species within 21 days, followed by a slower, and only partial, transformation to S-coordinated Sb(III) species (Figure S26 and Table S12). Formation of both O- and S-coordinated Sb(III) has also been observed during the reduction of Sb(V)-bearing

Figure 7. Bioreactors 21 d after inoculation: reddish-brown (A), black (B); dark orange (C); and charcoal gray (D).

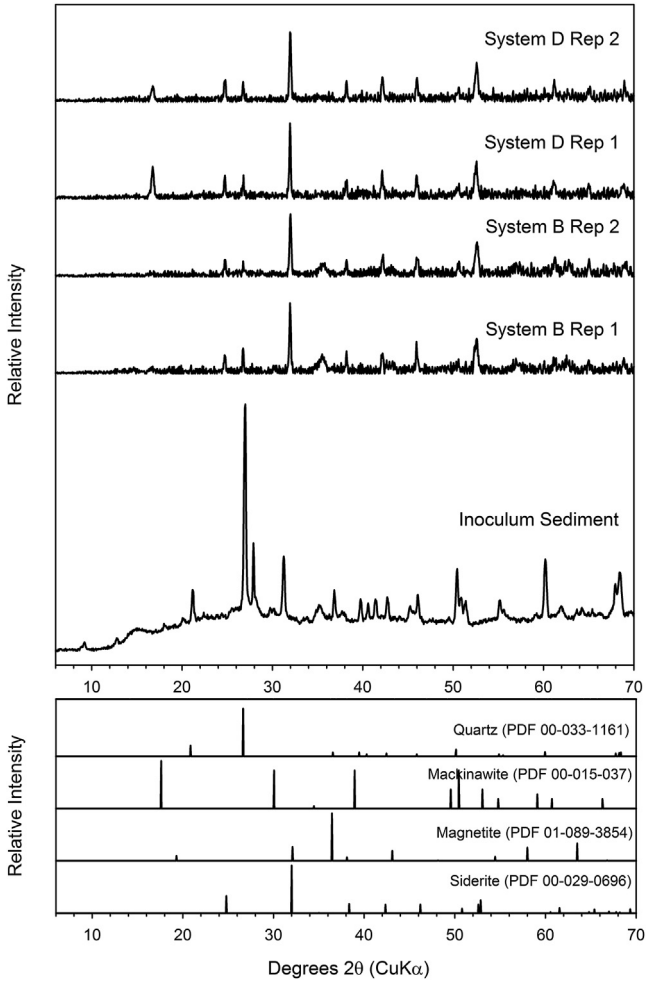

Figure 8. pXRD analysis of the inoculum sediment and the solids in each replicate bottles of system B [Fe(III) and sulfate] and D [Sb(V), Fe(III), and sulfate] 21 d after inoculation.

ferrihydrite by the abiotic addition of sulfide (Hockmann et al., 2020). Very little, if any, change in the spectra is observed beyond day 98, suggesting that this partitioning between O- and S-coordinated Sb(III) species is stable at least until day 570. It is possible that the mineral kermisite precipitated (which has both O- and S-coordinated Sb(III)),

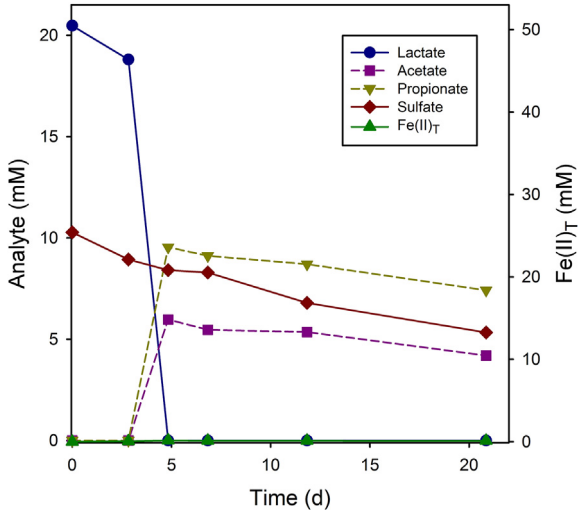

Figure 9. Concentration profiles of $Fe(II)_T$, sulfate, lactate, propionate, and acetate in system C [Fe(III) and sulfate] bioreactors.

thus fixing the aqueous Sb(III) concentration and correspondingly the proportion of Sb(III) adsorbed to the solids. It was not possible to resolve these scenarios further with the EXAFS analysis and the available standards.

3.2. Abiotic Reduction of Sb(V) by Fe(II)-Bearing minerals

Both mackinawite and sulfate green rust were effective at removing >99% of Sb from solution over 21 days (Figure 17). In the case of mackinawite, removal of Sb(V) from solution occurred via reduction to Sb(III) and precipitation of amorphous Sb_2S_3 (Figure 18). This result is similar to the findings of Kirsch et al. (2008) indicating reduction of Sb(V) to a highly-disordered or nanoparticulate Sb_2S_3 phase by mackinawite; furthermore, their Cryo-X-ray photoelectron spectroscopy results indicate that the reduction of Sb(V) was coupled to both the oxidation of Fe(II) to Fe(III) and S(-II) to S(0). In contrast to mackinawite, the removal of Sb(V) from solution by green rust was not accompanied by reduction to Sb(III) (Figure 18). The Fourier transformed Sb EXAFS spectrum from the GR system shows significant similarity to the aqueous $Sb(OH)_6^-$ spectrum up to R+Δ ~ 3.2 Å, suggesting that Sb is sequestered as an outer-sphere complex (Figure S27). Our spectrum lacks the signal near R+Δ ~ 2.8 Å observed previously from Sb–Fe coordination in an

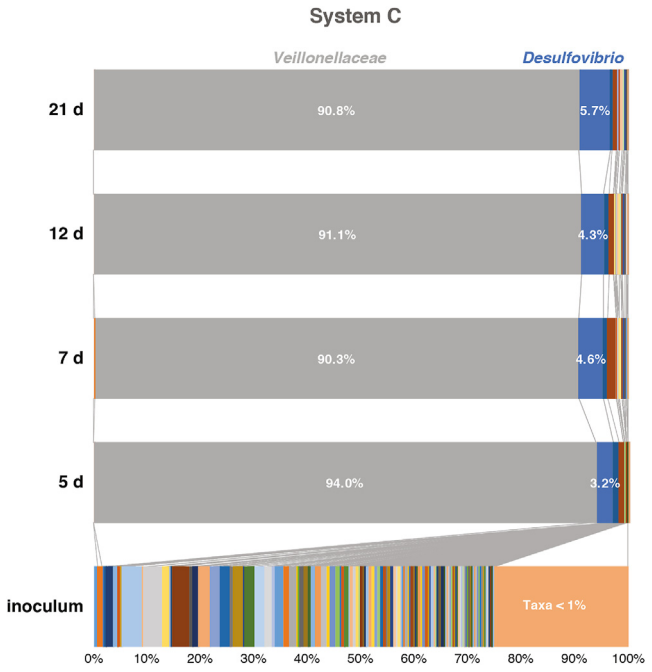

Figure 10. Changes in 16S rRNA gene-based community composition highlighting populations that are >5% at any time in system C [Sb(V) and sulfate].

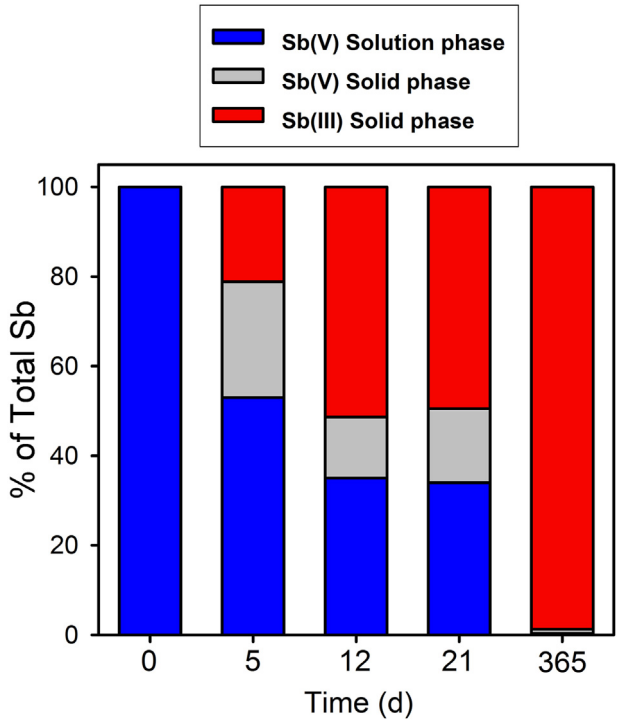

Figure 11. Distribution of Sb among solution and solid phases in system C. The valence state of Sb in the solid phase is based on linear combination fits of the Sb EXAFS spectra (Figure S23 and Table S10).

edge-sharing complex with green rust ((Mitsunobu et al., 2009), $R_{Sb\text{-}Fe}$ ~ 3.1 Å) or that from a corner-sharing complex of Sb(V) with soils ((Scheinost et al., 2006), $R_{Sb\text{-}Fe}$ ~ 3.6 Å). Our Sb(V)-green rust spectrum shows additional peak amplitude near R+Δ ~ 3.7 Å relative to the aqueous standard that could be fit with an Sb shell at 4.02 Å (Figure S27, Table S13). These fitting results can be rationalized by an ion exchange uptake mechanism, whereby $Sb(OH)_6^-$ anions replace SO_4^{2-} and form a

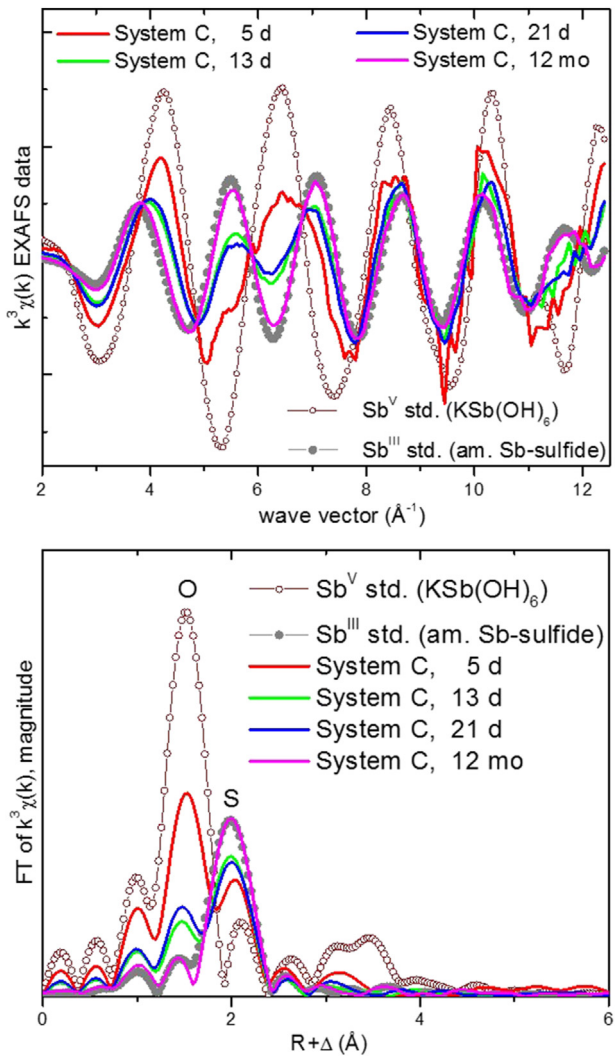

Figure 12. k^3-weighed EXAFS data (top) and Fourier transform (bottom) from subsamples of system C collected over time. The samples show a decrease in the O shell amplitude and increase in the S shell amplitude over time, corresponding to the change of coordination from Sb^V–O_6 to Sb^{III}–S. The proportions of the two components over time are quantified by LC fits of the data (Figure S23).

loose polynuclear network in the interlayer space (Figure S27). A peak corresponding to the Sb shell fit here was also present in the EXAFS data of Mitsunobu et al. (2009) but was not analyzed; their study also suggested anion exchange sequestration of Sb(V) based on the observed interlayer distance decrease with increasing Sb concentration. Although our results and those of Mitsunobu et al. (2009) show no reduction of Sb(V) by sulfate green rust, an earlier study by Mitsunobu et al. (2008) reported partial reduction of Sb(V) to Sb(III), ostensibly by sulfate green rust.

Magnetite and siderite were far less effective at removing Sb from solution compared to mackinawite and green rust, with nearly half remaining in solution after 21 d (Figure 17). Sb XANES analysis of the solids in each of these systems does not indicate Sb(III) formation above the ±5% uncertainty of the technique (Figures 17 and 18). Kirsch et al. (2009) also observed no reduction of Sb(V) (0.1 mM) by siderite (10 g L^{-1}, 86 mM Fe(II)) at near neutral pH; however, they report complete reduction of Sb(V) to Sb(III) by magnetite (0.1 mM Sb(V)); 3 g L^{-1} magnetite (13 mM Fe(II); pH ~7.7) within 7 d (Kirsch et al., 2008). The differences in the reactivity of magnetite with respect to Sb(V) reduction in our work and that of Kirsch et al. are consistent with variability in the redox reactivity of magnetite, that in some cases is attributable to differences in the Fe(II) content of the material (Gorski et al., 2010; Latta

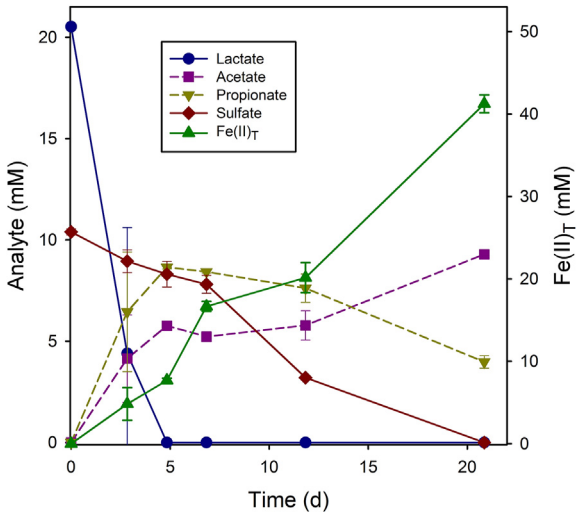

Figure 13. Concentration profiles of $Fe(II)_T$, sulfate, lactate, propionate, and acetate in system D [Fe(III) and sulfate] bioreactors. Error bars indicate the standard error.

et al., 2012; Pasakarnis et al., 2013). The Sb(V) EXAFS spectra from the magnetite and siderite systems are very similar and both exhibit suppression of the main O peak amplitude relative to the aqueous $Sb(OH)_6^-$ standard (Figure S28). Fits of this peak indicate increased disorder in the octahedral O shell relative to the aqueous species, consistent with inner-sphere complexation or precipitation as the sequestration mechanism (Figure S28 and Table S14). Relatively minor features are observed in the outer shell region ($R+\Delta = 2.5–4.0$ Å), where Fe or Sb shells typically contribute when Sb is in adsorption complexes or in precipitates (see e.g. Figure S27). The data were most simply reproduced with an Sb shell at ~3.6 Å, which corresponds to the Sb–Sb distance in the structure of tripuhyite (Figure S28 and Table S14). However, fits of these weak signals with other combinations of Fe and/or Sb shells corresponding to adsorption or incorporation complexes could not be statistically excluded, so the identity of the binding sites or of the precipitate could not be ascertained from the outer-shell EXAFS data. Based on the increased disorder in the near-neighbor O shell we speculate that aqueous Sb(V) was sequestered as an inner-sphere complex on the magnetite and siderite surfaces and/or it formed a surface precipitate. Our Sb(V) speciation results differ from those in Kirsch et al. (2008), where a much stronger signal from an Fe shell was observed and attributed to an edge-sharing complex with magnetite. Possible reasons for the differences include pH (pH 4.7–5.6 vs. pH 7 here), the surface properties of nanoparticulate magnetite vs. the regular magnetite used here, Sb:solids ratio (0.1 mM Sb vs 2 mM Sb here), and the measurement temperature—unlike our room temperature measurements, the spectra in Kirsch et al. (2008) were taken at 15 K, which may have enhanced the signal from the Fe shell or may have shifted the Sb(V) distribution in the solids towards the edge-sharing species.

Significantly less Sb(V) was removed from solution in the vivianite suspension, with only 29% uptake over 21 d (Figure 17). The edge position of the Sb XANES spectrum of the solids-associated Sb is at a slightly lower energy than the Sb(V) standard (Figure 18), and LC fitting of the EXAFS spectrum resulted in the determination of ~11% Sb(III) (Figure S30 and Table S16). The EXAFS data show similarity to the Sb minerals Sb_2O_5 and stibiconite [$Sb^{3+}Sb_2^{5+}O_6(OH)$] and the fits demonstrate the presence of significant Sb–Sb coordination at 3.79 Å (Figure S29 and Table S15). Therefore, the removal of Sb(V) from solution in the vivianite system is mostly due to the precipitation of Sb(V) mineral(s) that have a defined Sb–Sb coordination at ~3.8 Å. Although the bulk solution conditions are undersaturated with respect to Sb(V) mineral formation, it is possible that vivianite induces surface-enhanced precipitation. The reasons why vivianite enhances precipitation of Sb(V)

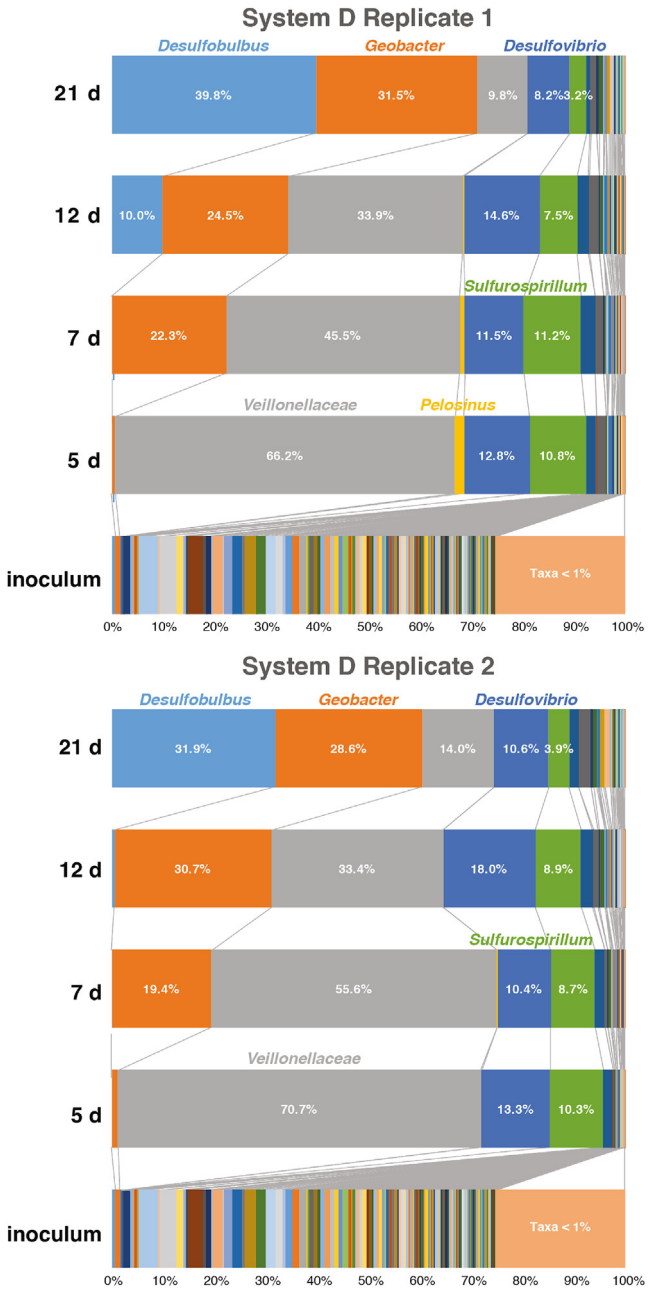

Figure 14. Changes in 16S rRNA gene-based community composition highlighting populations that are >5% at any time in system D [Sb(V), Fe(III), and sulfate].

while siderite and magnetite do not is unclear; possible reasons include differences in specific surface area, concentration of the surface sites, strength of the surface bond with Sb, or surface charge. It is also possible that the small amount of Sb(III) determined by XANES in the vivianite system induced the precipitation of stibiconite, with the remainder of Sb(V) being present as adsorbed or other mineralized Sb(V) species.

In addition to single-phase Fe(II)-bearing minerals, we assessed the potential for abiotic reduction of Sb(V) by reductants formed during DIR and DSR in the bioreactors by reacting Sb(V) with a subsample of suspension taken from system B (which initially contained Fe(III) and sulfate, but not Sb) 21 d after inoculation and pasteurized at 70 °C for 1 h. As previously noted, LC fitting of the Fe EXAFS spectrum of the solids in system B indicate that siderite comprises 52% of the Fe, with the remainder consisting of mackinawite (26%) and magnetite (22%). After reacting for an additional 21 d with Sb(V), the EXAFS spectrum of Sb in

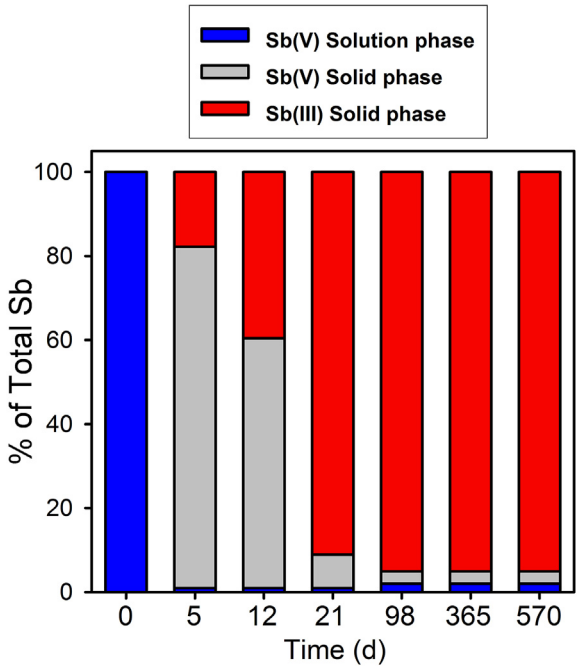

Figure 15. Distribution of Sb among solution and solid phases in system D. The valence state of Sb in the solid phase are based on linear combination fits of the Sb EXAFS spectra (Figure S26 and Table S12).

the pasteurized system B was intermediate between Sb(III) adsorbed to ferrihydrite and Sb(III)-sulfide (Figure 18). The EXAFS data from the Sb-amended pasteurized system B solids are similar to those from system D at 98 d, indicating a decrease in the peak corresponding to Sb(III)–O coordination and an increase in the peak corresponding to Sb(III)–S coordination (Figure S31). LC analysis of the data indicated that the Sb(III) in the pasteurized system B is comprised of a mixture of O- and S-coordinated species (70% and 30%, respectively, as determined by LC fitting using spectra of Sb(III) sorbed to ferrihydrite and the amorphous Sb(III) sulfide standard, Figure S31).

4. Discussion

4.1. Microbial community development and biogeochemical trajectories

Microbial community structure as represented by non-metric dimensional scaling indicated that the bacterial communities in systems B and D evolved over time following parallel trajectories, while the community in system C remained relatively unchanged (Figure 19). The microbial inoculum was initially highly diverse, but the experimental systems were quickly dominated (i.e. taxa present at >5% at any time) by members of the *Veillonellaceae* family (maximum 94%), as well as species of *Pelosinus* (maximum 6%), *Desulfovibrio* (maximum 39%), *Sulfurospirillum* (maximum 15%), *Geobacter* (maximum 32%), and *Desulfobulbus* (maximum 40%). Overall, the progression of the communities in systems B and D followed similar trajectories; i.e., an initial dominance by *Veillonellaceae* together with a significant presence of *Desulfovibrio* and *Sulfurospirillum*, followed by an ingrowth of *Geobacter* and *Desulfobulbus*. As the only difference between systems B and D is the addition of 2 mM Sb(V) to system D bioreactors, the presence of Sb does not appear to have had a substantial effect on the overall composition and trajectories of the microbial communities. Between either experimental systems or replicate treatments, there were substantial differences in the distribution of individual OTUs within the *Veillonellaceae* family and species of *Geobacter,* and relatively minor differences among members of the *Desulfovibrionaceae* family and species of *Desulfobulbus*; *Sulfurospirillum* was dominated by only a single OTU (Figure 20).

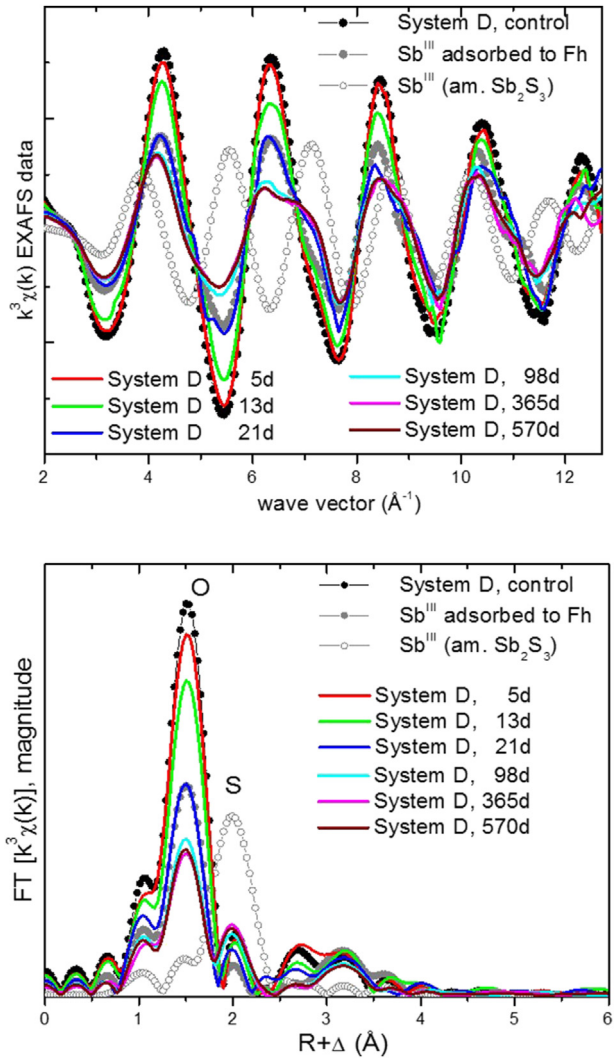

Figure 16. k^3-weighed EXAFS data (top) and Fourier transform (bottom) from subsamples of system D collected over time. The data from the reactor at 5 days is nearly identical to the uninoculated control, indicating lack of Sb^V reduction. Samples at later time show a decrease in the O shell amplitude, corresponding to the change of coordination from Sb^V–O_6 to Sb^{III}–O_3. The additional decrease at later times in the O shell amplitude and the relative increase in the amplitude where the S shell contributes (R+Δ = 2.0 Å) indicate the appearance of Sb^{III}–S coordination. The proportion of spectral components corresponding to the observed trends are quantified in LC fits of the data (Figure S26).

The biogeochemical trajectories observed in the bioreactors resulted from tight coupling of microbial processes involving C, S, and Fe. In all the inoculated bioreactors (systems B, C, and D), lactate concentrations dropped below detection (50 μM) within 5 d. Much of the lactate consumption can be attributed to lactate fermentation (Rx 1)

$$3CH_3CHOHCOO^- \rightarrow 2CH_3CH_2COO^- + CH_3COO^- + HCO_3^- + H^+ \quad (1)$$

as shown by the concentrations of propionate and acetate produced concomitant with the emergence of members of the *Veillonellaceae* (a family containing many lactate-fermenting species (Marchandin and Jumas-Bilak 2014)) in systems B, C, and D, and *Pelosinus* in system B (Shelobolina et al., 2007; Moe et al., 2012). In addition to serving as a substrate for lactate-fermenting bacteria, lactate can also be used as an electron donor for DIR and DSR (as can the products of lactate fermentation - acetate and propionate); however, an initial dominance of lactate-fermenting bacteria has been observed in other studies involving

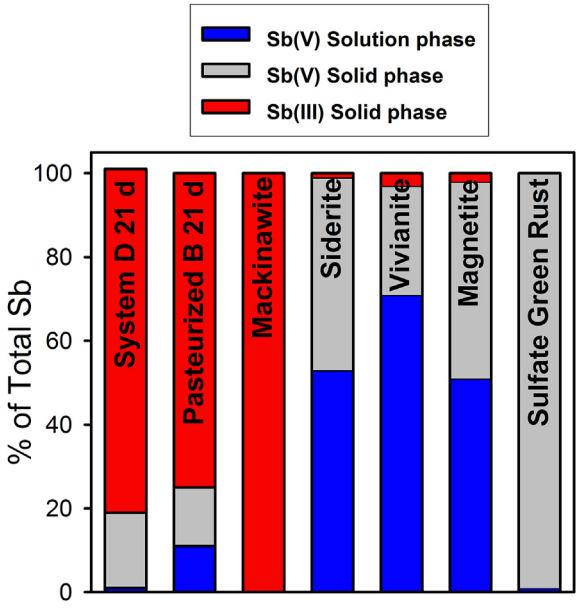

Figure 17. Distribution of Sb among solution and solid phases in the abiotic reactors. The valence state of Sb in the solid phase is based on linear combination fits of the Sb EXAFS spectra (Figures S30 and Table S16).

bioreactors where lactate was provided as the electron donor for DIR/DSR (Handley et al., 2014; Kwon et al. 2014, 2016).

Although systems B, C, and D displayed similar lactate consumption profiles, the profiles of Fe(II) production and sulfate consumption differed substantially. In system B bioreactors (containing Fe(III) and sulfate), 52% of Fe(III) was reduced to Fe(II) and 49% of sulfate was consumed within the first 5 d, compared to 15% and 18%, respectively, in system D bioreactors (containing Sb(V), Fe(III), and sulfate); 18% of sulfate was consumed within 5 d in system C bioreactors (containing Sb(V) and sulfate). In addition to members of the *Veillonellaceae*, there were significant increases in the relative abundance of OTUs belonging to the family *Desulfovibrionaceae* and the genus *Sulfurospirillum* in system B and D bioreactors and a substantially lower relative increase in *Desulfovibrionaceae* in system C. *Veillonellaceae* are not know to use either Fe(III) or sulfate as terminal electron acceptors for anaerobic respiration, so it is unlikely that they had a direct role in Fe(III) or sulfate reduction in the bioreactors. However, *Desulfovibrio* species use lactate an electron donor for DSR, and several *Desulfovibrio* species are able to reduce both Fe(III) to Fe(II) and S(0) to S(-II) (although this is typically not coupled to growth) and to ferment lactate (Kuever 2014). *Sulfurospirillum* species are not DSRB, but most species can respire using S(0) as an electron acceptor and lactate as an electron donor (Sorokin et al., 2013).

After day 5 and through day 21, the relative abundance of OTUs identified as *Geobacter* and *Desulfobulbus* increased substantially in system B and D bioreactors, concurrent with a relative decrease in *Veillonellaceae*. *Geobacter* are well-known DIRB and many species are also able to use S(0) (but not sulfate) as a terminal electron acceptor for anaerobic respiration (Röling 2014). Although some *Geobacter* species can use lactate as an electron donor, all known *Geobacter* isolates can use acetate and their initial increase in relative abundance in system B and D bioreactors was concurrent with the production of acetate (and propionate) from lactate fermentation. *Desulfobulbus* are DSRB that couple the reduction of sulfate, thiosulfate, and sulfite to sulfide to the incomplete oxidation of electron donors including lactate and propionate (Kuever 2014). Unlike the dynamic communities in system B and D bioreactors, the community in system C was relatively stable from day 5 through day 21, during which time the relative abundance of OTUs assigned to *Veillonellaceae* ranged from 90-94% and *Desulfovibrio* ranged from 3-6%. Although *Desulfovibrio* persist in all the bioreactors after lactate is

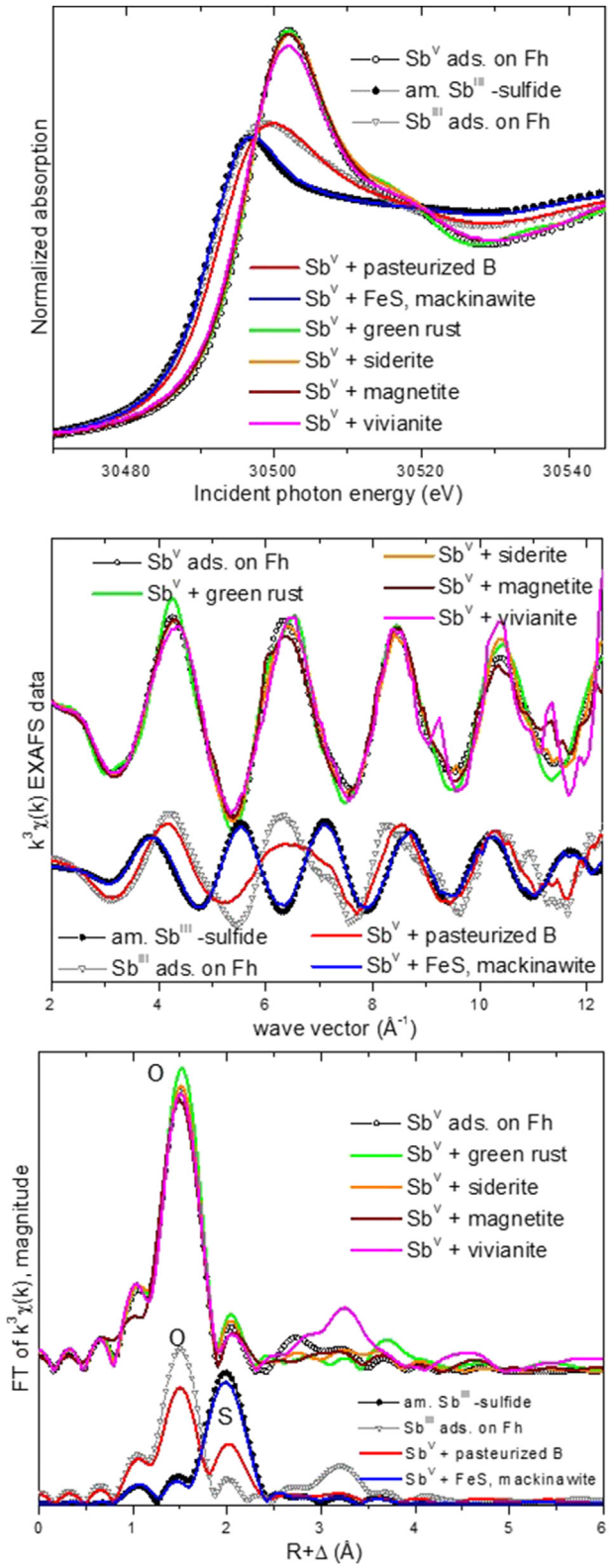

Figure 18. Sb XANES data from the abiotic reactors and the pasteurized system B reactor, compared to Sb(V) and Sb(III) standards (top) and k^3-weighed EXAFS data (middle) and Fourier transform (bottom) from the abiotic reactors. In the systems containing sulfide, the data are similar to O- or S- coordinated Sb(III); in the systems without sulfide, the data are similar to the standard of Sb(V) adsorbed on Fh. Further analysis of these data is presented in the SI.

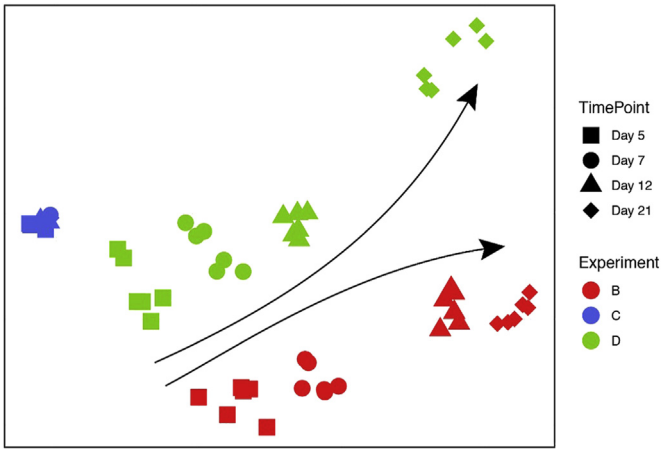

Figure 19. Nonmetric multidimensional scaling (NMDS) of microbial communities over time in bioreactors B (Fe(III) and sulfate), C (Sb(V) and sulfate), and D (Sb(V), Fe(III), and sulfate). Each symbol represents the microbial community from each system at a specific time and the arrows are a guide showing increasing reaction time.

depleted within the first 5 d, it is unlikely that they contribute to the removal of sulfate beyond day 5, as known species of *Desulfovibrio* are not able to use either acetate or propionate as electron donors for DSR (Kuever 2014).

4.2. Dynamics of Fe(III) and sulfate reduction

Our results suggest a strong coupling of Fe(III) and sulfate reduction in the bioreactors. Fe XANES analysis indicated a similar extent of Fe(III) reduction in system B (80 ± 5%) and D (71 ± 5%) bioreactors 21 d after inoculation. The potential for direct microbial Fe(III) reduction in these bioreactors is indicated by the relative enrichment of bacteria known to reduce Fe(III) (*Geobacter* species, in particular). However, aside from potential lactate-fermenting bacteria (*Veillonellaceae* and *Pelosinus*), the majority of the enriched microbes (defined here as taxa present at ≥ 5% relative abundance at any point during the experiment) belong to taxa known to reduce sulfate, thiosulfate, or S(0) to sulfide; specifically *Desulfovibrio*, *Sulfurospririllum*, *Desulfobulbus*, and *Geobacter*. Sulfide can reduce Fe(III) oxides, resulting in the oxidation of sulfide to S(0) (Rx. 2) (as molecular S(0) and polysulfides) and lesser amounts of thiosulfate, and the precipitation of ferrous sulfide phases (Rx. 3) (Pyzik and Sommer 1981; Dos Santos Afonso and Stumm 1992; Poulton 2003; Kwon et al., 2014), providing a means for indirect microbial reduction of Fe(III) in the bioreactors.

$$Fe(OH)_3(s) + HS^- + 2H^+ \rightarrow S^0 + Fe^{2+} + 3H_2O \quad (2)$$

$$Fe^{2+} + HS^- \rightarrow FeS(s) + H^+ \quad (3)$$

Indeed, the activity of DSRB has been shown to enhance Fe(III) oxide reduction (Li et al., 2006; Kwon et al., 2014; Hansel et al., 2015). The formation of S(0) and thiosulfate from the abiotic reduction of Fe(III) oxide by sulfide, which can be used as electron acceptors for anaerobic respiration, allows for active redox cycling of S. Furthermore, in the presence of S(0)-reducing bacteria, S(0) can act as an electron shuttle thereby enhancing the reduction of Fe(III) oxides (Nevin and Lovley 2000; Straub and Schink 2004; Haveman et al., 2008; Flynn et al., 2014; Berg et al., 2019).

Fe and S dynamics between system B and system D differed substantially, particularly during the first 7 d. During this time the rates of Fe(II) production and sulfate consumption were 6.16 ± 0.62 mM Fe(II) d^{-1} and -0.83 ± 0.20 mM SO_4^{2-} d^{-1} in system B compared to 2.31 ± 0.47 mM Fe(II) d^{-1} and -0.38 ± 0.05 mM SO_4^{2-} d^{-1} in system D. Given that system B and D bioreactors were identical except for the addition of 2

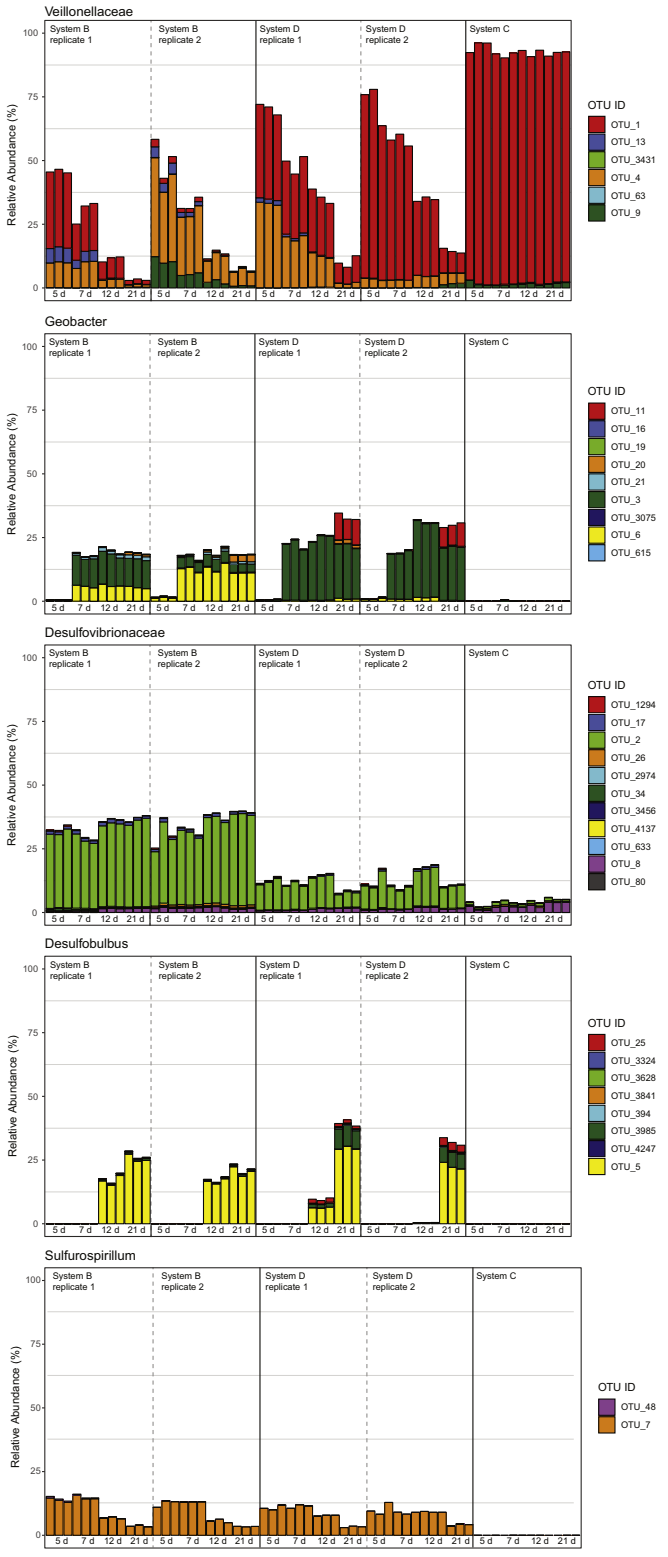

Figure 20. Relative abundance of operational taxonomic units (OTUs) classified as *Veillonellaceae*, *Geobacter*, *Desulfovibrionaceae*, *Desulfobulbus*, and *Sulfurospirillum* over time in bioreactors B (Fe(III) and sulfate), C (Sb(V) and sulfate), and D (Sb(V), Fe(III), and sulfate).

mM $KSb(OH)_6$ to system D, the lower rates of Fe(III) and sulfate reduction in system D bioreactors may have been due to the presence of Sb. The sorption of oxyanions such as phosphate, arsenate, and silicate on Fe(III) oxides has been shown to decrease the rate of biotic and abiotic reduction of Fe(III) oxides (Amirbahman et al., 1997; O'Loughlin et al., 2010;

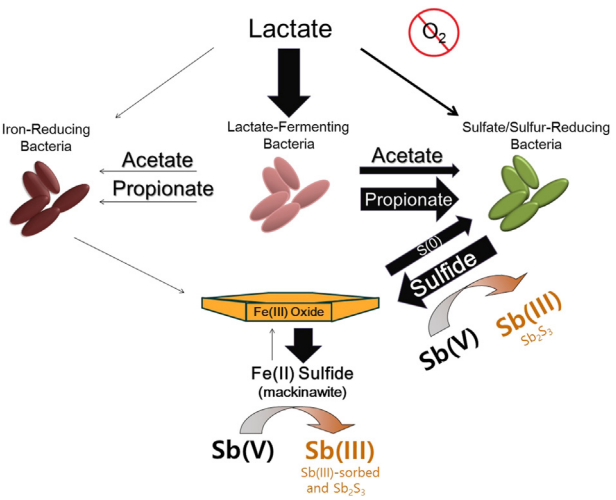

Figure 21. Conceptual model of the highly coupled biogeochemical dynamics of C, S, and Fe leading to Sb(V) reduction in system D.

Sergent et al., 2011; Gomez et al., 2013) as well as suppressing the formation of magnetite as a secondary mineral during microbial reduction of Fe(III) oxides (Fredrickson et al., 1998; Kukkadapu et al., 2004; Borch et al., 2007; O'Loughlin et al., 2010; Sergent et al., 2011). Similar to phosphate and arsenate, antimonate sorbs to ferrihydrite and other Fe(III) oxides (Tighe et al., 2005; Mitsunobu et al., 2010; Guo et al., 2014), such that sorption of antimonate may have decreased the rate of Fe(II) production in system D bioreactors relative to system B and may also account for the lack of magnetite formation in system D. Accumulation of sulfide can inhibit DSR (McCartney and Oleszkiewicz 1991; Reis et al., 1992; Icgen and Harrison 2006), however reaction of sulfide with Fe(III) in the bioreactors provides a sink for sulfide, potentially reducing sulfide toxicity. Because the sorption of phosphate on ferrihydrite significantly decreases the reactivity of ferrihydrite with sulfide (Poulton et al., 2002), sorption of antimonate on ferrihydrite in system D bioreactors may make ferrihydrite a less efficient sink for sulfide, which could in turn lead to a slower rate of sulfate reduction in system D compared to system B. Despite the initial inhibition of Fe(II) production and sulfate consumption in the presence of Sb(V), by day 21 both system B and D bioreactors have reached similar endpoints; i.e., sulfate is depleted in both systems and the distribution of Fe phases as determined by Fe EXAFS is similar (comprising 59%/52% siderite and 26%/18% mackinawite, and 23% magnetite/ferrihydrite in systems B/D, respectively).

4.3. Pathways(s) of Sb(V) reduction in the bioreactors

The reduction of Sb(V) to Sb(III) in the bioreactors may have resulted from both direct microbial reduction and coupled biotic/abiotic processes. Our attempts to enrich for Sb(V)-reducing bacteria were unsuccessful; however, this does not preclude the potential for direct microbial reduction in the bioreactors. The reduction of Sb(V) to Sb(III) was observed in both the absence (system C) and presence (system D) of Fe(III) oxide (ferrihydrite). In the system C bioreactor, sulfate consumption by DSRB was concurrent with the formation of Sb_2S_3, consistent with the reduction of Sb(V) and formation of Sb_2S_3 by dissolved sulfide (Polack et al., 2009). The presence of ferrihydrite in the system D bioreactors creates the potential for additional pathways for Sb(V) reduction. The reduction of ferrihydrite (either by DIRB or by sulfide) can lead to the formation of a suite of Fe(II)-bearing minerals including magnetite, siderite, vivianite, green rust, and ferrous sulfide (e.g., mackinawite) (Fredrickson et al., 1998; Cantrell et al., 2003). Of these potential Fe(II)-bearing secondary minerals, only siderite and mackinawite were observed in system D. In our abiotic Sb(V) reduction experiments, siderite was ineffective at reducing Sb(V), but complete reduction to Sb(III) was observed in the presence of mackinawite. Sb EXAFS analysis of Sb speciation in the solids in system D bioreactors indicated that 92% of the Sb(V) was reduced to Sb(III) within 21 d, with 85% of the Sb(III) having O as the nearest neighbor based on a standard of Sb(III) adsorbed to ferrihydrite and 7% present as amorphous Sb_2S_3; after 1 year of incubation 67% was present as Sb(III)–O and 30% as Sb_2S_3 (Table S12). The extent of Sb(V) reduction and the speciation of Sb(III) in system D was similar to that in pasteurized material collected from system B (at day 21) amended with 2 mM Sb(V); i.e., 67% of the Sb(V) was reduced to Sb(III) within 21 d, with 70% of the Sb(III) being O-coordinated species and 30% as amorphous Sb_2S_3. These results suggest that Sb(V) reduction in system D bioreactors was primarily the result of abiotic reduction by sulfide species.

Overall, the reduction of Sb(V) in the bioreactors was highly coupled with the dynamics of C, S, and Fe (Figure 21). Lactate was consumed primarily by lactate-fermenting bacteria (based on the stoichiometry of propionate production), although it is likely that some lactate was utilized by DSRB and DIRB. Propionate and acetate were utilized by DSRB and DIRB for reduction of sulfate and Fe(III) after lactate was consumed. Ferrihydrite was reduced both by DIRB (e.g., *Geobacter* spp.) and by reaction with sulfide produced by sulfate- (and likely thiosulfate- and sulfur-) reducing bacteria. The products of this reaction were primarily siderite and mackinawite, with mackinawite serving as the primary reductant for the reduction of Sb(V) to Sb(III). In the absence of Fe(III), Sb(III) precipitated as Sb_2S_3; however in presence of residual ferrihydrite, Sb was present primarily as Sb(III) sorbed to ferrihydrite along with a lesser amount as Sb_2S_3.

4.4. Implications for Sb biogeochemistry

Sb(V)-reducing bacteria and archaea have been identified in, or isolated from, soils and sediments from a wide range of aquatic and terrestrial environments (Abin and Hollibaugh 2014; Kulp et al., 2014; Nguyen and Lee 2014; Lai et al. 2016, 2018; Nguyen et al., 2018; Wang et al., 2018; Zhang and Hu 2019), suggesting that direct (enzymatic) microbial reduction of Sb(V) may be a significant component of Sb biogeochemical cycling, particularly in environments with low S. Our results suggest that in natural and engineered environments with sufficient S to support active S redox cycling, Sb(V) reduction may be driven primarily by a coupled biotic-abiotic process wherein biogenic sulfide species are the primary reductants, which is consistent with similar observations from field and laboratory studies (Wang et al., 2013; Couture et al., 2015; Zhang et al., 2016; Liang et al., 2018). Moreover, our results also suggest that the presence of Fe(III) oxides in sulfidogenic environments can impact the distribution of Sb(III) species (e.g., sorbed Sb(III) versus Sb_2S_3 precipitation), which has implications for the fate and transport of Sb.

Declarations

Author contribution statement

Clayton R. Johnson & Edward J. O'Loughlin: Conceived and designed the experiments; Performed the experiments; Analyzed and interpreted the data; Contributed reagents, materials, analysis tools or data; Wrote the paper.

Dionysios A. Antonopoulos, Jason C. Koval & Kenneth M. Kemner: Analyzed and interpreted the data; Contributed reagents, materials, analysis tools or data.

Maxim I. Boyanov: Analyzed and interpreted the data; Contributed reagents, materials, analysis tools or data; Wrote the paper.

Theodore M. Flynn: Analyzed and interpreted the data.

Funding statement

This work under the Wetlands Hydrobiogeochemistry Scientific Focus Area (SFA) at Argonne National Laboratory was supported by Subsurface Biogeochemical Research Program, Office of Biological and Environmental Research (BER), Office of Science, United States Department of Energy (DOE) (DE-AC02- 06CH11357). MRCAT/EnviroCAT operations are supported by DOE and the member institutions. Use of the Advanced Photon Source, an Office of Science User Facility operated for the U.S. Department of Energy (DOE) Office of Science by Argonne National Laboratory, was supported by the U.S. DOE under Contract No. DE-AC02-06CH11357. Argonne National Laboratory is a U.S. DOE laboratory managed by UChicago Argonne, LLC. This work was supported in part by the U.S. DOE, Office of Science, Office of Workforce Development for Teachers and Scientists (WDTS) under the Science Undergraduate Laboratory Internships Program (SULI).

Data availability statement

Data associated with this study has been deposited at MG-RAST under project number 96966.

Declaration of interests statement

The authors declare no conflict of interest.

Additional information

Supplementary content related to this article has been published online at https://doi.org/10.1016/j.heliyon.2021.e06275.

Acknowledgements

We thank Bhoopesh Mishra, Drew Latta, the beamline staff for help during the XAFS data collection, and the anonymous reviewers for their thoughtful comments.

References

Abin, C.A., Hollibaugh, J.T., 2014. Dissimilatory antimonate reduction and production of antimony trioxide microcrystals by a novel microorganism. Environ. Sci. Technol. 48, 681–688.

Abin, C.A., Hollibaugh, J.T., 2017. *Desulfuribacillus stibiiarsenatis* sp. nov., an obligately anaerobic, dissimilatory antimonate- and arsenate-reducing bacterium isolated from anoxic sediments, and emended description of the genus *Desulfuribacillus*. Int. J. Syst. Evol. Microbiol. 67, 1011–1017.

Amirbahman, A., Sigg, L., van Gunten, U., 1997. Reductive dissolution of Fe(III) (hydr) oxides by cysteine: kinetics and mechanisms. J. Colloid Interface Sci. 194, 194–206.

Anderson, C.G., 2012. The metallurgy of antimony. Chemie der Erde - Geochemistry 72, 3–8.

Ankudinov, A.L., Ravel, B., Conradson, S.D., 1998. Real-space multiple-scattering calculation and interpretation of x-ray absorption near-edge structure. Phys. Rev. B 58, 7565–7576.

Arsic, M., Teasdale, P.R., Welsh, D.T., Johnston, S.G., Burton, E.D., Hockmann, K., Bennett, W.W., 2018. Diffusive gradients in thin films reveals differences in antimony and arsenic mobility in a contaminated wetland sediment during an oxic-anoxic transition. Environ. Sci. Technol. 52, 1118–1127.

Bates, S.T., Berg-Lyons, D., Caporaso, J.G., Walters, W.A., Knight, R., Fierer, N., 2011. Examining the global distribution of dominant archaeal populations in soil. ISME J. 5, 908–917.

Belzile, N., Chen, Y.-W., Wang, Z., 2001. Oxidation of antimony (III) by amorphous iron and manganese oxyhydroxides. Chem. Geol. 174, 379–387.

Berg, J.S., Jezequel, D., Duverger, A., Lamy, D., Laberty-Robert, C., Miot, J., 2019. Microbial diversity involved in iron and cryptic sulfur cycling in the ferruginous, low-sulfate waters of Lake Pavin. PloS One 14, e0212787.

Berlepsch, P., Armbruster, T., Brugger, J., Criddle, A.J., Graeser, S., 2003. Tripuhyite, $FeSbO_4$, revisited. Mineral. Mag. 67, 31–46.

Bolanz, R.M., Bläss, U., Ackermann, S., Ciobotă, V., Rösch, P., Tarcea, N., Popp, J., Majzlan, J., 2013. The effect of antimonate, arsenate, and phosphate on the transformation of ferrihydrite to goethite, hematite, feroxyhyte, and tripuhyite. Clay Clay Miner. 61, 11–25.

Borch, T., Masue, Y., Kukkadapu, R.K., Fendorf, S., 2007. Phosphate imposed limitations on biological reduction and alteration of ferrihydrite. Environ. Sci. Technol. 41, 166–172.

Boyanov, M.I., Kemner, K.M., 2019. Application of synchrotron x-ray absorption spectroscopy and microscopy techniques to the study of biogeochemical processes. In: Kenney, J.P.L., Veeramani, H., Alessi, D.S. (Eds.), Analytical Geomicrobiology: A Handbook of Instrumental Techniques. Cambridge University Press, pp. 238–261.

Burton, E.D., Hockmann, K., Karimian, N., Johnston, S.G., 2019. Antimony mobility in reducing environments: the effect of microbial iron(III)-reduction and associated secondary mineralization. Geochim. Cosmochim. Acta 245, 278–289.

Cantrell, K.J., Yabusaki, S.B., Engelhard, M.H., Mitroshkov, A.V., Thornton, E.C., 2003. Oxidation of H2S by iron oxides in unsaturated conditions. Environ. Sci. Technol. 37, 2192–2199.

Caporaso, J.G., Kuczynski, J., Stombaugh, J., Bittinger, K., Bushman, F.D., Costello, E.K., Fierer, N., Pena, A.G., Goodrich, J.K., Gordon, J.I., Huttley, G.A., Kelley, S.T., Knights, D., Koenig, J.E., Ley, R.E., Lozupone, C.A., McDonald, D., Muegge, B.D., Pirrung, M., Reeder, J., Sevinsky, J.R., Turnbaugh, P.J., Walters, W.A., Widmann, J., Yatsunenko, T., Zaneveld, J., Knight, R., 2010. QIIME allows analysis of high-throughput community sequencing data. Nat. Methods 7, 335–336.

Caporaso, J.G., Lauber, C.L., Walters, W.A., Berg-Lyons, D., Huntley, J., Fierer, N., Owens, S.M., Betley, J., Fraser, L., Bauer, M., Gormley, N., Gilbert, J.A., Smith, G., Knight, R., 2012. Ultra-high-throughput microbial community analysis on the Illumina HiSeq and MiSeq platforms. ISME J. 6, 1621–1624.

Caporaso, J.G., Lauber, C.L., Walters, W.A., Berg-Lyons, D., Lozupone, C.A., Turnbaugh, P.J., Fierer, N., Knight, R., 2011. Global patterns of 16S rRNA diversity at a depth of millions of sequences per sample. Proc. Natl. Acad. Sci. U. S. A. 108 (Suppl 1), 4516–4522.

Courtin-Nomade, A., Rakotoarisoa, O., Bril, H., Grybos, M., Forestier, L., Foucher, F., Kunz, M., 2012. Weathering of Sb-rich mining and smelting residues: insight in solid speciation and soil bacteria toxicity. Chemie der Erde - Geochemistry 72, 29–39.

Couture, R.M., Charlet, L., Markelova, E., Made, B., Parsons, C.T., 2015. On-off mobilization of contaminants in soils during redox oscillations. Environ. Sci. Technol. 49, 3015–3023.

Dos Santos Afonso, M., Stumm, W., 1992. Reductive dissolution of iron(III) (hydr)oxides by hydrogen sulfide. Langmuir 8, 1671–1675.

Dupont, D., Arnout, S., Jones, P.T., Binnemans, K., 2016. Antimony recovery from end-of-life products and industrial process residues: a critical review. J. Sustain. Metal. 2, 79–103.

Edgar, R.C., 2010. Search and clustering orders of magnitude faster than BLAST. Bioinformatics 26, 2460–2461.

Edgar, R.C., 2013. UPARSE: highly accurate OTU sequences from microbial amplicon reads. Nat. Methods 10, 996–998.

Filella, M., Belzile, N., Chen, Y.-W., 2002. Antimony in the environment: a review focused on natural waters. I. Occurrence. Earth Sci. Rev. 57, 125–176.

Filella, M., Belzile, N., Lett, M.-C., 2007. Antimony in the environment: a review focused on natural waters. III. Microbiota relevant interactions. Earth Sci. Rev. 80, 195–217.

Filella, M., May, P.M., 2003. Computer simulation of the low-molecular-weight inorganic species distribution of antimony(III) and antimony(V) in natural waters. Geochim. Cosmochim. Acta 67, 4013–4031.

Filella, M., Williams, P.A., Belzile, N., 2009. Antimony in the environment: knowns and unknowns. Environ. Chem. 6, 95.

Flynn, T.M., O'Loughlin, E.J., Mishra, B., DiChristina, T.J., Kemner, K.M., 2014. Sulfur-mediated electron shuttling during bacterial iron reduction. Science 344, 1039–1042.

Fredrickson, J.K., Zachara, J.M., Kennedy, D.W., Dong, H., Onstott, T.C., Hinman, N.W., Li, S.-M., 1998. Biogenic iron mineralization accompanying the dissimilatory reduction of hydrous ferric oxide by a groundwater bacterium. Geochim. Cosmochim. Acta 62, 3239–3257.

Gomez, M.A., Jim Hendry, M., Hossain, A., Das, S., Elouatik, S., 2013. Abiotic reduction of 2-line ferrihydrite: effects on adsorbed arsenate, molybdate, and nickel. RSC Adv. 3, 25812–25822.

Gorski, C.A., Nurmi, J.T., Tratnyek, P.G., Hofstetter, T.B., Scherer, M.M., 2010. Redox behavior of magnetite: implications for contaminant reduction. Environ. Sci. Technol. 44, 55–60.

Guo, X., Wang, K., He, M., Liu, Z., Yang, H., Li, S., 2014. Antimony smelting process generating solid wastes and dust: characterization and leaching behaviors. J. Environ. Sci. (China) 26, 1549–1556.

Guo, X., Wu, Z., He, M., Meng, X., Jin, X., Qiu, N., Zhang, J., 2014. Adsorption of antimony onto iron oxyhydroxides: adsorption behavior and surface structure. J. Hazard Mater. 276, 339–345.

Hamady, M., Lozupone, C., Knight, R., 2010. Fast UniFrac: facilitating high-throughput phylogenetic analyses of microbial communities including analysis of pyrosequencing and PhyloChip data. ISME J. 4, 17–27.

Handley, K.M., Wrighton, K.C., Miller, C.S., Wilkins, M.J., Kantor, R.S., Thomas, B.C., Williams, K.H., Gilbert, J.A., Long, P.E., Banfield, J.F., 2014. Disturbed subsurface microbial communities follow equivalent trajectories despite different structural starting points. Environ. Microbiol. 17, 622–636.

Hansel, C.M., Lentini, C.J., Tang, Y., Johnston, D.T., Wankel, S.D., Jardine, P.M., 2015. Dominance of sulfur-fueled iron oxide reduction in low-sulfate freshwater sediments. ISME J. 9, 2400–2412.

Haveman, S.A., DiDonato Jr., R.J., Villanueva, L., Shelobolina, E.S., Postier, B., Xu, B., Liu, A., Lovley, D.R., 2008. Genome-wide gene expression patterns and growth requirements suggest that *Peolobacter carbinolicus* reduces Fe(III) indirectly via sulfide production. Appl. Environ. Microbiol. 74, 4277–4284.

He, M., Wang, N., Long, X., Zhang, C., Ma, C., Zhong, Q., Wang, A., Wang, Y., Pervaiz, A., Shan, J., 2018. Antimony speciation in the environment: recent advances in understanding the biogeochemical processes and ecological effects. J. Environ. Sci. 75, 14–39.

Herath, I., Vithanage, M., Bundschuh, J., 2017. Antimony as a global dilemma: geochemistry, mobility, fate and transport. Environ. Pollut. 223, 545–559.

Hockmann, K., Lenz, M., Tandy, S., Nachtegaal, M., Janousch, M., Schulin, R., 2014. Release of antimony from contaminated soil induced by redox changes. J. Hazard Mater. 275, 215–221.
Hockmann, K., Planer-Friedrich, B., Johnston, S.G., Peiffer, S., Burton, E.D., 2020. Antimony mobility in sulfidic systems: coupling with sulfide-induced iron oxide transformations. Geochem. Cosmochim. Acta 282, 276–296.
Icgen, B., Harrison, S., 2006. Exposure to sulfide causes populations shifts in sulfate-reducing consortia. Res. Microbiol. 157, 784–791.
Johnston, S.G., Bennett, W.W., Doriean, N., Hockmann, K., Karimian, N., Burton, E.D., 2020. Antimony and arsenic speciation, redox-cycling and contrasting mobility in a mining-impacted river system. Sci. Total Environ. 710, 136354.
Karimian, N., Johnston, S.G., Burton, E.D., 2018. Antimony and arsenic partitioning during Fe(2+)-induced transformation of jarosite under acidic conditions. Chemosphere 195, 515–523.
Karimian, N., Johnston, S.G., Burton, E.D., 2018. Iron and sulfur cycling in acid sulfate soil wetlands under dynamic redox conditions: a review. Chemosphere 197, 803–816.
Kirsch, R., Scheinost, A.C., Charlet, L., 2009. Reaction of antimony with nano-particulate magnetite, mackinawite and siderite—an EXAFS investigation. In: FZD—IRC Annual Report 2008. Bernhard G. Dresden Germany. Forschungzentrum Dresden Institute of Radiochemistry, p. 53.
Kirsch, R., Scheinost, A.C., Rossberg, A., Banerjee, D., Charlet, L., 2008. Reduction of antimony by nano-particulate magnetite and mackinawite. Mineral. Mag. 72, 185–189.
Kolmert, Å., Wikström, P., Hallberg, K.B., 2000. A fast and simple turbidimetric method for the determination of sulfate in sulfate-reducing bacterial cultures. J. Microbiol. Methods 41, 179–184.
Kropf, A.J., Katsoudas, J., Chattopadhyay, S., Shibata, T., Lang, E.A., Zyryanov, V.N., Ravel, B., McIvor, K., Kemner, K.M., Scheckel, K.G., Bare, S.R., Terry, J., Kelly, S.D., Bunker, B.A., Segre, C.U., Garrett, R., Gentle, I., Nugent, K., Wilkins, S., 2010. The new MRCAT (Sector 10) bending magnet beamline at the Advanced Photon Source. AIP Conf. Proc. 1234, 299–302.
Kuever, J., 2014. The family *Desulfobulbaceae*. In: Dworkin, M. (Ed.), The Prokaryotes. Springer-Verlag, Berlin Heidelburg, pp. 75–86.
Kuever, J., 2014. The family *Desulfovibrionaceae*. In: Dworkin, M. (Ed.), The Prokaryotes. Springer-Verlag, Berlin Heidelburg, pp. 107–133.
Kukkadapu, R.K., Zachara, J.M., Fredrickson, J.K., Kennedy, D.W., 2004. Biotransformation of two-line silica-ferrihydrite by a dissimilatory Fe(III)-reducing bacterium: formation of carbonate green rust in the presence of phosphate. Geochim. Cosmochim. Acta 68, 2799–2814.
Kulp, T.R., Miller, L.G., Braiotta, F., Webb, S.M., Kocar, B.D., Blum, J.S., Oremland, R.S., 2014. Microbiological reduction of Sb(V) in anoxic freshwater sediments. Environ. Sci. Technol. 48, 218–226.
Kwon, M.J., Boyanov, M.I., Antonopoulos, D.A., Brulc, J.M., Johnston, E.R., Skinner, K.A., Kemner, K.M., O'Loughlin, E.J., 2014. Effects of dissimilatory sulfate reduction on FeIII (hydr)oxide reduction and microbial community development. Geochim. Cosmochim. Acta 129, 4570–4576.
Kwon, M.J., O'Loughlin, E.J., Boyanov, M.I., Brulc, J.M., Johnston, E.R., Kemner, K.M., Antonopoulos, D.A., 2016. Impact of organic carbon electron donors on microbial community development under iron- and sulfate-reducing conditions. PloS One 1–22.
Kwon, M.J., Yang, J.-S., Shim, M.J., Boyanov, M.I., Kemner, K.M., O'Loughlin, E.J., 2014. Acid extraction overestimates the total Fe(II) in the presence of iron (hydr)oxide and sulfide minerals. Environ. Sci. Technol. Lett. 1, 310–314.
Lai, C.Y., Dong, Q.Y., Rittmann, B.E., Zhao, H.P., 2018. Bioreduction of antimonate by anaerobic methane oxidation in a membrane biofilm batch reactor. Environ. Sci. Technol. 52, 8693–8700.
Lai, C.Y., Wen, L.L., Zhang, Y., Luo, S.S., Wang, Q.Y., Luo, Y.H., Chen, R., Yang, X., Rittmann, B.E., Zhao, H.P., 2016. Autotrophic antimonate bio-reduction using hydrogen as the electron donor. Water Res. 88, 467–474.
Latta, D.E., Gorski, C.A., Boyanov, M.I., O'Loughlin, E.J., Kemner, K.M., Scherer, M.M., 2012. Influence of magnetite stoichiometry on U^{VI} reduction. Environ. Sci. Technol. 46, 778–786.
Leuz, A.-K., Mönch, H., Johnson, C.A., 2006. Sorption of Sb(III) and Sb(V) to goethite: influence on Sb(III) oxidation and mobilization. Environ. Sci. Technol. 40, 7277–7282.
Li, J., Wang, Q., Oremland, R.S., Kulp, T.R., Rensing, C., Wang, G., 2016. Microbial antimony biogeochemistry: enzymes, regulation, and related metabolic pathways. Appl. Environ. Microbiol. 82, 5482–5495.
Li, Y.-L., Vali, H., Yang, J., Phelps, T.J., Zhang, C.L., 2006. Reduction of iron oxides enhanced by a sulfate-reducing bacterium and biogenic H_2S. Geomicrobiol. J. 23, 103–117.
Lialikova, N.N., 1974. *Stibiobacter senarmontii*: a new microorganism oxidizing antimony. Microbiologiia 43, 941–943.
Liang, Zw, Zs, Hua, Jia, P., Liu, J., Luo, Zh, Chen, Wc, Kuang, Jl, Liao, B., Shu, Ws, Li, Jt, 2018. Strong associations between biogeochemical factors and Sb species in sediments of the world's largest Sb mine (xikuangshan) in China. J. Geophys. Res.: Biogeosciences 123, 1548–1556.
Liu, F., Zhang, G., Liu, S., Fu, Z., Chen, J., Ma, C., 2018. Bioremoval of arsenic and antimony from wastewater by a mixed culture of sulfate-reducing bacteria using lactate and ethanol as carbon sources. Int. Biodeterior. Biodegrad. 126, 152–159.
Lozupone, C., Lladser, M.E., Knights, D., Stombaugh, J., Knight, R., 2011. UniFrac: an effective distance metric for microbial community comparison. ISME J. 5, 169–172.
Marchandin, H., Jumas-Bilak, E., 2014. The family Veillonellaceae. In: Dworkin, M. (Ed.), The Prokaryotes. Springer-Verlag, Berlin Heidelburg, pp. 433–453.
McCartney, D.M., Oleszkiewicz, J.A., 1991. Sulfide inhibition of anaerobic degradation of lactate and acetate. Water Res. 25, 203–209.
McComb, K.A., Craw, D., McQuillan, A.J., 2007. ATR-IR spectroscopic study of antimonate adsorption to iron oxide. Langmuir 23, 12125–12130.
McMurdie, P.J., Holmes, S., 2013. phyloseq: an R package for reproducible interactive analysis and graphics of microbiome census data. PloS One 8, e61217.
Meyer, F., Paarmann, D., D'Souza, M., Olson, R., Glass, E.M., Kubal, M., Paczian, T., Rodriguez, A., Stevens, R., Wilke, A., Wilkening, J., Edwards, R.A., 2008. The metagenomics RAST server - a public resource for the automatic phylogenetic and functional analysis of metagenomes. BMC Bioinf. 9, 386.
Mitsunobu, S., Harada, T., Takahashi, Y., 2006. Comparison of antimony behavior with that of arsenic under various soil redox conditions. Environ. Sci. Technol. 40, 7270–7276.
Mitsunobu, S., Muramatsu, C., Watanabe, K., Sakata, M., 2013. Behavior of antimony(V) during the transformation of ferrihydrite and its environmental implications. Environ. Sci. Technol. 47, 9660–9667.
Mitsunobu, S., Takahashi, Y., Sakai, Y., 2008. Abiotic reduction of antimony(V) by green rust ($Fe_4(II)Fe_2(III)(OH)_{12}SO_4$ * $3H_2O$). Chemoshpere 70, 942–947.
Mitsunobu, S., Takahashi, Y., Sakai, Y., Inumaru, K., 2009. Interaction of synthetic sulfate green rust with antimony(V). Environ. Sci. Technol. 43, 318–323.
Mitsunobu, S., Takahashi, Y., Terada, Y., Sakata, M., 2010. Antimony(V) incorporation into synthetic ferrihydrite, goethite, and natural iron oxyhydroxides. Environ. Sci. Technol. 44, 3712–3718.
Moe, W.M., Stebbing, R.E., Rao, J.U., Bowman, K.S., Nobre, M.F., da Costa, M.S., Rainey, F.A., 2012. *Pelosinus defluvii* sp. nov., isolated from chlorinated solvent-contaminated groundwater, emended description of the genus *Pelosinus* and transfer of *Sporotalea propionica* to *Pelosinus propionicus* comb. nov. Int. J. Syst. Evol. Microbiol. 62, 1369–1376.
Murciego, A.M., Sanchez, A.G., Gonzalez, M.A., Gil, E.P., Gordillo, C.T., Fernandez, J.C., Triguero, T.B., 2007. Antimony distribution and mobility in topsoils and plants (*Cytisus striatus, Cistus ladanifer* and *Dittrichia viscosa*) from polluted Sb-mining areas in Extremadura (Spain). Environ. Pollut. 145, 15–21.
Nevin, K.P., Lovley, D.R., 2000. Potential for nonenzymatic reduction of Fe(III) via electron shuttling in subsurface sediments. Environ. Sci. Technol. 34, 2472–2478.
Newville, M., Livinš, P., Yacoby, Y., Rehr, J.J., Stern, E.A., 1993. Near-edge x-ray absorption fine structure of Pb: a comparison of theory and experiment. Phys. Rev. B 47, 14126–14131.
Newville, M., Ravel, B., Haskel, D., Stern, E.A., 1995. Analysis of multiple scattering XAFS data using theoretical standards. Physica B 208/209, 154–156.
Nguyen, V.K., Choi, W., Park, Y., Yu, J., Lee, T., 2018. Characterization of diversified Sb(V)-reducing bacterial communities by various organic or inorganic electron donors. Bioresour. Technol. 250, 239–246.
Nguyen, V.K., Lee, J.-U., 2014. Isolation and characterization of antimony-reducing bacteria from sediments collected in the vicinity of an antimony factory. Geochem. J. 31, 855–861.
Nguyen, V.K., Park, Y., Lee, T., 2019. Microbial antimonate reduction with a solid-state electrode as the sole electron donor: a novel approach for antimony bioremediation. J. Hazard Mater. 377, 179–185.
O'Loughlin, E.J., Burris, D.R., 2004. Reduction of halogenated ethanes by green rust. Environ. Toxicol. Chem. 23, 41–48.
O'Loughlin, E.J., Gorski, C., Scherer, M.M., Boyanov, M.I., Kemner, K.M., 2010. Effects of oxyanions, natural organic matter, and cell density on the bioreduction of lepidocrocite (γ-FeOOH) and secondary mineral formation. Environ. Sci. Technol. 44, 4570–4576.
O'Loughlin, E.J., Gorski, C.A., Flynn, T.M., Scherer, M.M., 2019. Electron donor utilization and secondary mineral formation during the bioreduction of lepidocrocite by *Shewanella putrefaciens* CN32. Minerals 9.
O'Loughlin, E.J., Kelly, S.D., Csencsits, R., Cook, R.E., Kemner, K.M., 2003. Reduction of uranium(VI) by mixed iron(II)/iron(III) hydroxide (green rust): formation of UO_2 nanoparticles. Environ. Sci. Technol. 37, 721–727.
Okkenhaug, G., Grasshorn Gebhardt, K.A., Amstaetter, K., Bue, H.L., Herzel, H., Mariussen, E., Rossebo Almas, A., Cornelissen, G., Breedveld, G.D., Rasmussen, G., Mulder, J., 2016. Antimony (Sb) and lead (Pb) in contaminated shooting range soils: Sb and Pb mobility and immobilization by iron based sorbents, a field study. J. Hazard Mater. 307, 336–343.
Oremland, R., 2016. Geomicrobial interactions with arsenic and antimony. In: Ehrlich, H.L., Newman, D.K., Kappler, A. (Eds.), Ehrlich's Geomicrobiology. CRC Press Taylor & Francis Group, Boca Raton, FL, pp. 297–321.
Park, S.-C., Boyanov, M.I., Kemner, K.M., O'Loughlin, E.J., Kwon, M.J., 2021. Distribution and speciation of Sb and toxic metal(loid)s near an antimony refinery and their effects on indigenous microorganisms. J. Hazard Mater. 403, 123625.
Pasakarnis, T.S., Boyanov, M.I., Kemner, K.M., Mishra, B., O'Loughlin, E.J., Parkin, G., Scherer, M.M., 2013. Influence of chloride and Fe(II) content on the reduction of Hg(II) by magnetite. Environ. Sci. Technol. 47, 6987–6994.
Patterson, R.R., Fendorf, S.E., Fendorf, M.J., 1997. Reduction of hexavalent chromium by amorphous iron sulfide. Environ. Sci. Technol. 31, 2039–2044.
Planer-Friedrich, B., Scheinost, A.C., 2011. Formation and structural characterization of thioantimony species and their natural occurrence in geothermal waters. Environ. Sci. Technol. 45, 6855–6863.
Polack, R., Chen, Y.-W., Belzile, N., 2009. Behaviour of Sb(V) in the presence of dissolved sulfide under controlled anoxic aqueous conditions. Chem. Geol. 262, 179–185.
Poulton, S.W., 2003. Sulfide oxidation and iron dissolution kinetics during the reaction of dissolved sulfide with ferrihydrite. Chem. Geol. 202, 79–94.
Poulton, S.W., Krom, M.D., Van Rijn, J., Raiswell, R., 2002. The use of hydrous iron (III) oxides for the removal of hydrogen sulphide in aqueous systems. Water Res. 36, 825–834.

Pyzik, A.J., Sommer, S.E., 1981. Sedimentary iron monosulfides: kinetics and mechanism of formation. Geochim. Cosmochim. Acta 45, 687–698.
Qi, P., Pichler, T., 2016. Sequential and simultaneous adsorption of Sb(III) and Sb(V) on ferrihydrite: implications for oxidation and competition. Chemosphere 145, 55–60.
Qi, P., Pichler, T., 2017. Competitive adsorption of As(III), As(V), Sb(III) and Sb(V) onto ferrihydrite in multi-component systems: implications for mobility and distribution. J. Hazard Mater. 330, 142–148.
Quast, C., Pruesse, E., Yilmaz, P., Gerken, J., Schweer, T., Yarza, P., Peplies, J., Glockner, F.O., 2013. The SILVA ribosomal RNA gene database project: improved data processing and web-based tools. Nucleic Acids Res. 41, D590–D596.
Ravel, B., Newville, M., 2005. Athena, artemis, hephaestus: data analysis for X-ray absorption. J. Synchrotron Radiat. 12, 537–541.
Reis, M.A., Almeida, J.S., Lemos, P.C., Carrondo, M.J., 1992. Effect of hydrogen sulfide on growth of sulfate reducing bacteria. Biotechnol. Bioeng. 40, 593–600.
Ren, M., Ding, S., Fu, Z., Yang, L., Tang, W., Tsang, D.C.W., Wang, D., Wang, Y., 2019. Seasonal antimony pollution caused by high mobility of antimony in sediments: in situ evidence and mechanical interpretation. J. Hazard Mater. 367, 427–436.
Ritchie, V.J., Ilgen, A.G., Mueller, S.H., Trainor, T.P., Goldfarb, R.J., 2013. Mobility and chemical fate of antimony and arsenic in historic mining environments of the Kantishna Hills district, Denali National Park and Preserve, Alaska. Chem. Geol. 335, 172–188.
Röling, W.F.M., 2014. The family geobacteraceae. In: Dworkin, M. (Ed.), The Prokaryotes. Springer-Verlag, Berlin Heidelburg, pp. 157–172.
Scheinost, A.C., Rossberg, A., Vantelon, D., Xifra, I., Kretzschmar, R., Leuz, A.-K., Funke, H., Johnson, C.A., 2006. Quantitative antimony speciation in shooting-range soils by EXAFS spectroscopy. Geochim. Cosmochim. Acta 70, 3299–3312.
Schwertmann, U., Cornell, R.M., 2000. Iron Oxides in the Laboratory. Wiley-VCH, Weinheim.
Sergent, A.-S., Jorand, F., Hanna, K., 2011. Effects of Si-bearing minerals on the nature of secondary iron mineral products from lepidocrocite bioreduction. Chem. Geol. 289, 86–97.
Shangguan, Y., Qin, X., Zhao, L., Wang, L., Hou, H., 2015. Effects of iron oxide on antimony(V) adsorption in natural soils: transmission electron microscopy and X-ray photoelectron spectroscopy measurements. J. Soils Sediments 16, 509–517.
Shangguan, Y.X., Zhao, L., Qin, Y., Hou, H., Zhang, N., 2016. Antimony release from contaminated mine soils and its migration in four typical soils using lysimeter experiments. Ecotoxicol. Environ. Saf. 133, 1–9.
Shelobolina, E.S., Nevin, K.P., Blakeney-Hayward, J.D., Johnsen, C.V., Plaia, T.W., Krader, P., Woodard, T., Holmes, D.E., VanPraagh, C.G., Lovley, D.R., 2007. *Geobacter pickeringii* sp. nov., *Geobacter argillaceus* sp. nov. and *Pelosinus fermentans* gen. nov., sp. nov., isolated from subsurface kaolin lenses. Int. J. Syst. Evol. Microbiol. 57, 126–135.
Sørensen, J., 1982. Reduction of ferric iron in anaerobic, marine sediment and interaction with reduction of nitrate and sulfate. Appl. Environ. Microbiol. 43, 319–324.
Sorokin, D.Y., Tourova, T.P., Muyzer, G., 2013. Isolation and characterization of two novel alkalitolerant sulfidogens from a Thiopaq bioreactor, Desulfonatronum alkalitolerans sp. nov., and Sulfurospirillum alkalitolerans sp. nov. Extremophiles 17, 535–543.
Stookey, L.L., 1970. Ferrozine-A new spectrophotometric reagent for iron. Anal. Chem. 42, 779–781.
Straub, K.L., Schink, B., 2004. Ferrihydrite-dependent growth of *Sulfurospirillum deleyianum* through electron transfer via sulfur cycling. Appl. Environ. Microbiol. 70, 5744–5749.
USGS, 2020. Mineral Commodity Summaries 2020. U.S. Geological Survey, p. 200.
Tandy, S., Hockmann, K., Keller, M., Studer, B., Papritz, A., Schulin, R., 2017. Antimony mobility during prolonged waterlogging and reoxidation of shooting range soil: a field experiment. Sci. Total Environ. 624, 838–844.
Tandy, S., Meier, N., Schulin, R., 2017. Use of soil amendments to immobilize antimony and lead in moderately contaminated shooting range soils. J. Hazard Mater. 324, 617–625.
Terry, L.R., Kulp, T.R., Wiatrowski, H., Miller, L.G., Oremland, R.S., 2015. Microbiological oxidation of antimony(III) with oxygen or nitrate by bacteria isolated from contaminated mine sediments. Appl. Environ. Microbiol. 81, 8478–8488.
Thompson, L.R., Sanders, J.G., McDonald, D., Amir, A., Ladau, J., Locey, K.J., Prill, R.J., Tripathi, A., Gibbons, S.M., Ackermann, G., Navas-Molina, J.A., Janssen, S., Kopylova, E., Vazquez-Baeza, Y., Gonzalez, A., Morton, J.T., Mirarab, S., Zech Xu, Z., Jiang, L., Haroon, M.F., Kanbar, J., Zhu, Q., Jin Song, S., Kosciolek, T., Bokulich, N.A., Lefler, J., Brislawn, C.J., Humphrey, G., Owens, S.M., Hampton-Marcell, J., Berg-Lyons, D., McKenzie, V., Fierer, N., Fuhrman, J.A., Clauset, A., Stevens, R.L., Shade, A., Pollard, K.S., Goodwin, K.D., Jansson, J.K., Gilbert, J.A., Knight, R., Earth Microbiome Project, C., 2017. A communal catalogue reveals Earth's multiscale microbial diversity. Nature 551, 457–463.
Tighe, M., Lockwood, P., Wilson, S., 2005. Adsorption of antimony(V) by floodplain soils, amorphous iron(III) hydroxide and humic acid. J. Environ. Monit. 7, 1177–1185.
Ullrich, M.K., Pope, J.G., Seward, T.M., Wilson, N., Planer-Friedrich, B., 2013. Sulfur redox chemistry governs diurnal antimony and arsenic cycles at Champagne Pool, Waiotapu, New Zealand. J. Volcanol. Geoth. Res. 262, 164–177.
Vithanage, M., Rajapaksha, A.U., Dou, X., Bolan, N.S., Yang, J.E., Ok, Y.S., 2013. Surface complexation modeling and spectroscopic evidence of antimony adsorption on iron-oxide-rich red earth soils. J. Colloid Interface Sci. 406, 217–224.
Wang, H., Chen, F., Mu, S., Zhang, D., Pan, X., Lee, D.J., Chang, J.S., 2013. Removal of antimony (Sb(V)) from Sb mine drainage: biological sulfate reduction and sulfide oxidation-precipitation. Bioresour. Technol. 146, 799–802.
Wang, L., Ye, L., Yu, Y., Jing, C., 2018. Antimony redox biotransformation in the subsurface: effect of indigenous Sb(V) respiring microbiota. Environ. Sci. Technol. 52, 1200–1207.
Warnken, J., Ohlsson, R., Welsh, D.T., Teasdale, P.R., Chelsky, A., Bennett, W.W., 2017. Antimony and arsenic exhibit contrasting spatial distributions in the sediment and vegetation of a contaminated wetland. Chemosphere 180, 388–395.
Whitten, A.E., Dittrich, B., Spackman, M.A., Turner, P., Brown, T.C., 2004. Charge density analysis of two polymorphs of antimony(III) oxide. Dalton Trans. 23–29.
Wolin, E.A., Wolin, M.J., Wolfe, R.S., 1963. Formation of methane by bacterial extracts. J. Biol. Chem. 238, 2882–2886.
Yang, Z., Hosokawa, H., Sadakane, T., Kuroda, M., Inoue, D., Nishikawa, H., Ike, M., 2020. Isolation and characterization of facultative-anaerobic antimonate-reducing bacteria. Microorganisms 8, 1435.
Zhang, G., Ouyang, X., Li, H., Fu, Z., Chen, J., 2016. Bioremoval of antimony from contaminated waters by a mixed batch culture of sulfate-reducing bacteria. Int. Biodeterior. Biodegrad. 115, 148–155.
Zhang, H., Hu, X., 2019. Bioadsorption and microbe-mediated reduction of Sb(V) by a marine bacterium in the presence of sulfite/thiosulfate and the mechanism study. Chem. Eng. J. 359, 755–764.
Zhang, J., Kobert, K., Flouri, T., Stamatakis, A., 2014. PEAR: a fast and accurate Illumina Paired-End reAd mergeR. Bioinformatics 30, 614–620.
Zhu, Y., Wu, M., Gao, N., Chu, W., An, N., Wang, Q., Wang, S., 2018. Removal of antimonate from wastewater by dissimilatory bacterial reduction: role of the coexisting sulfate. J. Hazard Mater. 341, 36–45.
Zhuang, W., Lai, X., Wang, Q., Liu, Y., Chen, Q., Liu, C., 2018. Distribution characteristics, sources and ecological risk of antimony in the surface sediments of Changjiang Estuary and the adjacent sea, East China. Mar. Pollut. Bull. 137, 474–480.